2024

UNCOVER Spectroscopy Confirms the Surprising Ubiquity of Active Galactic Nuclei in Red Sources at z > 5

Sam E. Cutler

John R. Weaver

Katherine E. Whitaker

et. al.

The Astrophysical Journal, 964:39 (18pp), 2024 March 20 https://doi.org/10.3847/1538-4357/ad1e5f

UNCOVER Spectroscopy Confirms the Surprising Ubiquity of Active Galactic Nuclei in Red Sources at $z > 5$

Jenny E. Greene[1], Ivo Labbe[2], Andy D. Goulding[1], Lukas J. Furtak[3], Iryna Chemerynska[4], Vasily Kokorev[5], Pratika Dayal[5], Marta Volonteri[4], Christina C. Williams[6,7], Bingjie Wang (王冰洁)[8,9,10], David J. Setton[1,31], Adam J. Burgasser[11], Rachel Bezanson[12], Hakim Atek[4], Gabriel Brammer[13], Sam E. Cutler[14], Robert Feldmann[15], Seiji Fujimoto[16,32], Karl Glazebrook[17], Anna de Graaff[18], Gourav Khullar[12], Joel Leja[8,9,10], Danilo Marchesini[19], Michael V. Maseda[20], Jorryt Matthee[21,22], Tim B. Miller[23,24], Rohan P. Naidu[25,33], Themiya Nanayakkara[17], Pascal A. Oesch[13,26], Richard Pan[19], Casey Papovich[27,28], Sedona H. Price[12], Pieter van Dokkum[29], John R. Weaver[14], Katherine E. Whitaker[14,30], and Adi Zitrin[3]

[1] Department of Astrophysical Sciences, Princeton University, 4 Ivy Lane, Princeton, NJ 08544, USA
[2] Centre for Astrophysics and Supercomputing, Swinburne University of Technology, Melbourne, VIC 3122, Australia
[3] Department of Physics, Ben-Gurion University of the Negev, P.O. Box 653, Beer-Sheva 84105, Israel
[4] Institut d'Astrophysique de Paris, CNRS, Sorbonne Université, 98bis Boulevard Arago, F-75014 Paris, France
[5] Kapteyn Astronomical Institute, University of Groningen, 9700 AV Groningen, The Netherlands
[6] NSFs National Optical-Infrared Astronomy Research Laboratory, 950 N. Cherry Avenue, Tucson, AZ 85719, USA
[7] Steward Observatory, University of Arizona, 933 North Cherry Avenue, Tucson, AZ 85721, USA
[8] Department of Astronomy & Astrophysics, The Pennsylvania State University, University Park, PA 16802, USA
[9] Institute for Computational & Data Sciences, The Pennsylvania State University, University Park, PA 16802, USA
[10] Institute for Gravitation and the Cosmos, The Pennsylvania State University, University Park, PA 16802, USA
[11] Department of Astronomy & Astrophysics, UC San Diego, La Jolla, CA 92093, USA
[12] Department of Physics and Astronomy and PITT PACC, University of Pittsburgh, Pittsburgh, PA 15260, USA
[13] Cosmic Dawn Center (DAWN), Niels Bohr Institute, University of Copenhagen, Jagtvej 128, København N, DK-2200, Denmark
[14] Department of Astronomy, University of Massachusetts, Amherst, MA 01003, USA
[15] Institute for Computational Science, University of Zurich, Zurich CH-8057, Switzerland
[16] Department of Astronomy, The University of Texas at Austin, Austin, TX 78712, USA
[17] Centre for Astrophysics and Supercomputing, Swinburne University of Technology, P.O. Box 218, Hawthorn, VIC 3122, Australia
[18] Max-Planck-Institut für Astronomie, Königstuhl 17, D-69117 Heidelberg, Germany
[19] Department of Physics & Astronomy, Tufts University, 574 Boston Avenue, Medford, MA 02155, USA
[20] Department of Astronomy, University of Wisconsin-Madison, 475 N. Charter Street, Madison, WI 53706 USA
[21] Department of Physics, ETH Zurich, Wolfgang-Pauli-Strasse 27, 8093 Zurich, Switzerland
[22] Institute of Science and Technology Austria (IST Austria), Am Campus 1, Klosterneuburg, Austria
[23] Department of Astronomy, Yale University, New Haven, CT 06511, USA
[24] Center for Interdisciplinary Exploration and Research in Astrophysics (CIERA) and Department of Physics & Astronomy, Northwestern University, IL 60201, USA
[25] MIT Kavli Institute for Astrophysics and Space Research, 77 Massachusetts Avenue, Cambridge, MA 02139, USA
[26] Department of Astronomy, University of Geneva, Chemin Pegasi 51, 1290 Versoix, Switzerland
[27] Department of Physics and Astronomy, Texas A&M University, College Station, TX 77843-4242 USA
[28] George P. and Cynthia Woods Mitchell Institute for Fundamental Physics and Astronomy, Texas A&M University, College Station, TX 77843-4242 USA
[29] Astronomy Department, Yale University, 52 Hillhouse Avenue, New Haven, CT 06511, USA
[30] Cosmic Dawn Center (DAWN), Denmark

Received 2023 September 11; revised 2024 January 9; accepted 2024 January 13; published 2024 March 13

Abstract

The James Webb Space Telescope is revealing a new population of dust-reddened broad-line active galactic nuclei (AGN) at redshifts $z \gtrsim 5$. Here we present deep NIRSpec/Prism spectroscopy from the Cycle 1 Treasury program Ultradeep NIRSpec and NIRCam ObserVations before the Epoch of Reionization (UNCOVER) of 15 AGN candidates selected to be compact, with red continua in the rest-frame optical but with blue slopes in the UV. From NIRCam photometry alone, they could have been dominated by dusty star formation or an AGN. Here we show that the majority of the compact red sources in UNCOVER are dust-reddened AGN: 60% show definitive evidence for broad-line Hα with a FWHM > 2000 km s $^{-1}$, 20% of the current data are inconclusive, and 20% are brown dwarf stars. We propose an updated photometric criterion to select red $z > 5$ AGN that excludes brown dwarfs and is expected to yield >80% AGN. Remarkably, among all $z_{\rm phot} > 5$ galaxies with F277W – F444W > 1 in UNCOVER at least 33% are AGN regardless of compactness, climbing to at least 80% AGN for sources with F277W – F444W > 1.6. The confirmed AGN have black hole masses of 10^7–10^9 $M_\odot$. While their UV luminosities ($-16 > M_{\rm UV} > -20$ AB mag) are low compared to UV-selected AGN at these epochs, consistent with percent-level

[31] Brinson Prize Fellow.
[32] Hubble Fellow.
[33] NASA Hubble Fellow.

scattered AGN light or low levels of unobscured star formation, the inferred bolometric luminosities are typical of 10^7–10^9 $M_\odot$ black holes radiating at ∼10%–40% the Eddington limit. The number densities are surprisingly high at $\sim 10^{-5}$ Mpc^{-3} mag^{-1}, 100 times more common than the faintest UV-selected quasars, while accounting for ∼1% of the UV-selected galaxies. While their UV faintness suggests they may not contribute strongly to reionization, their ubiquity poses challenges to models of black hole growth.

Unified Astronomy Thesaurus concepts: Active galactic nuclei (16); High-redshift galaxies (734)

1. Introduction

Over the past decade, large-area surveys have discovered hundreds of UV-luminous active galactic nuclei (AGN) at $z > 5$ (e.g., Mortlock et al. 2011; Bañados et al. 2018; Fan et al. 2019; Wang et al. 2021; Fan et al. 2023; Harikane et al. 2022). Unlike lower redshifts, the number densities of UV-selected AGN at $z > 5$ are not strongly luminosity dependent for $M_{\rm UV}$ fainter than ~ -25 mag (Matsuoka et al. 2018, 2023), while the galaxy luminosity function rises steeply, so that UV-selected AGN fainter than $M_{\rm UV} \approx -25$ mag make up <0.1% of the galaxy population at high redshift. Determining whether or not black hole growth is preceding or lagging galaxy growth at these epochs has important implications for the seeding and coevolution of black holes and galaxies (e.g., Volonteri & Reines 2016; Dayal et al. 2019; Greene et al. 2020; Inayoshi et al. 2020; Zhang et al. 2023a), for the sources of reionization (e.g., Madau & Haardt 2015; Dayal et al. 2020; Trebitsch et al. 2023), and potentially for the sources of gravitational waves (e.g., Amaro-Seoane et al. 2023; Somalwar & Ravi 2023).

With the advent of the James Webb Space Telescope (JWST; Gardner et al. 2023), we have begun to identify the heretofore missing UV-faint AGN. They have been discovered through broad Balmer lines (Übler et al. 2023; Barro et al. 2023; Harikane et al. 2023; Kocevski et al. 2023; Larson et al. 2023; Maiolino et al. 2023; Matthee et al. 2023; Oesch et al. 2023), from color and morphology (Endsley et al. 2022; Ono et al. 2023; Furtak et al. 2023a; Hainline et al. 2023a; Leung et al. 2023; Onoue et al. 2023; Yang et al. 2023), and from X-ray emission (Bogdan et al. 2024; Goulding et al. 2023). The number densities of these JWST-selected sources is roughly a few percent of the galaxy population, and while they are UV faint, their implied bolometric luminosities span a broad range ($L_{\rm bol} \sim 10^{43}$–10^{46} erg s^{-1}), implying a wide range of $M_{\rm BH} \sim 10^6$–10^9 $M_\odot$.

An interesting subcomponent of the JWST-selected AGN population is quite red (e.g., F2777 − F444W > 1; see also Fujimoto et al. 2022; Furtak et al. 2023a). For instance, Matthee et al. (2023) spectroscopically identified a sample of broad-line AGN that all appear as "little red dots" with steep red continua in the rest-frame optical (see also Kocevski et al. 2023). Other JWST- and broad-line-selected samples show large red fractions of 10%–20% (Harikane et al. 2023; Maiolino et al. 2023). We note that for $z > 4$, the JWST-based selections are at much bluer rest-frame wavelengths than previous mid-infrared-based methods (e.g., Stern et al. 2005; Donley et al. 2012; Assef et al. 2013). At lower redshift, reddened broad-line AGN are known (e.g., Glikman et al. 2012; Banerji et al. 2015), but they have particular spectral energy distributions (SEDs), with both a steep red optical continuum and an additional UV component, which are quite rare at lower redshift (e.g., Noboriguchi et al. 2019).

What has not been clear to date is whether a photometrically selected sample of compact red sources with a significant UV component is dominated by AGN as well, or whether they may be powered by star formation (Akins et al. 2023; Barro et al. 2023; Maiolino et al. 2023). Recently, we (Labbé et al. 2023a; L23 hereafter) published a large photometric sample of compact red sources from the Cycle 1 JWST program Ultradeep NIRSpec and NIRCam ObserVations before the Epoch of Reionization (UNCOVER; Bezanson et al. 2022). We have now obtained follow-up NIRSpec spectroscopy for 15 of the 40 galaxies presented in L23. Here, we explore the nature of the sample, and show that our selection indeed provides a very high yield of $z > 4$ AGN.

We present the UNCOVER data in Section 2, and review the photometric selection in Section 3. The spectroscopic analysis, and in particular the identification of broad Hα emission lines, is presented in Section 4. We present a revised selection for compact red sources in Section 5, and consider the physical implications of our results in Section 6. Throughout, we assume a concordance cosmology with $H_0 = 70$ km s^{-1} Mpc^{-1}, $\Omega_\Lambda = 0.7$, and $\Omega_M = 0.3$ (Hinshaw et al. 2013).

2. Data, Sample, and Spectroscopic Follow-up

In this section we briefly describe the UNCOVER survey (Section 2.1 Bezanson et al. 2022) and the Micro-Shutter Assembly (MSA)/PRISM spectroscopy and reductions in Section 2.2. Many exciting results have already come from the PRISM spectroscopy of the compact red sources, including a triply imaged $z = 7$ AGN (Furtak et al. 2023b), a broad-line AGN at $z = 8.5$ (Fujimoto et al. 2023a; Kokorev et al. 2023), and three brown dwarfs which show similar SEDs as red AGN (Burgasser et al. 2024; Langeroodi & Hjorth 2023). We have also reported two $z > 12$ galaxies (Wang et al. 2023), and some of the faintest known targets in the epoch of reionization (Atek et al. 2023a).

2.1. UNCOVER Photometry

Our search is performed using the JWST Cycle 1 Treasury program UNCOVER (Bezanson et al. 2022). UNCOVER imaging was completed in 2022 November, comprising ultradeep (29–30 AB mag) imaging over 45 arcmin^2 in the galaxy cluster A2744. This well-studied Frontier Field cluster (Lotz et al. 2017) at $z = 0.308$ has one of the largest high-magnification areas of known clusters, and thus made an excellent target for deep (4–6 hr per filter) imaging across seven NIRCam filters (F115W, F150W, F200W, F277W, F356W, F410M, and F444W). The nominal depth ∼ 30 mag can comfortably reach sources as faint as 31.5 mag with the help of magnification. Photometric catalogs (Weaver et al. 2024) including existing Hubble Space Telescope (HST) data have been made available to the public, and the lens model is also publicly available (Furtak et al. 2023c). The initial selection of objects is based on the UNCOVER Data Release 1 images and catalogs (Weaver et al. 2024).

Fujimoto et al. (2023b) present deep Atacama Large Millimeter/submillimeter Array (ALMA) 1.2 mm continuum

imaging of A2744. A wider, deeper 1.2 mm map of the full NIRCam UNCOVER area was newly obtained in Cycle 9 (#2022.1.00073.S; S. Fujimoto 2024, in preparation), reaching a continuum rms sensitivity of 33 μJy in the deepest areas. Prior-based photometry is extracted for all sources by measuring the ALMA flux in the natural resolution map (beam $\approx 0\farcs7$–$0\farcs8$) at the NIRCam positions.

The UNCOVER region additionally has full coverage with high spatial resolution X-ray imaging using the Chandra ACIS-I detector, which upon completion will have an ~2.3 Ms depth (PI: A. Bogdan). These X-ray data have already been used to identify the highest-redshift X-ray AGN to date, UHZ1, spectroscopically confirmed at $z = 10.1$ (Bogdan et al. 2024; Goulding et al. 2023).

2.2. PRISM Spectroscopy and Reductions

2.2.1. MSA Observational Setup

All 17 spectroscopic targets were observed with the MSA follow-up program of the UNCOVER JWST field A2744 (Bezanson et al. 2022). The UNCOVER NIRSpec/PRISM observations were taken over seven MSA configurations. These observations employed a "2-POINT-WITH-NIRCam-SIZE2" dither pattern and a three-shutter slit-let nod pattern at an aperture angle ~44°. The observational design for the photometric component is described in detail in Bezanson et al. (2022), the catalog is described by Weaver et al. (2024), the photometric redshifts are explored in some depth by Wang et al. (2024), and the spectroscopic experimental design and reductions are explained by S. H. Price et al. (2024, in preparation).

2.2.2. NIRSpec/PRISM Data Reduction

The data reduction is performed with `msaexp` (v0.6.10; Brammer 2022), beginning from the level 2 products downloaded from MAST.[34] `msaexp` then corrects for 1/f noise, masks snowballs, and removes the bias frame by frame. The JWST reduction pipeline is used to apply a world coordinate system correction to identify each slit, and then to perform flat-fielding and to apply photometric corrections. 2D slits are extracted and drizzled onto a common grid to make vertically shifted and stacked 2D spectra, to which a local background subtraction is applied. The optimal extraction uses a Gaussian model on the collapsed spectrum with a free center and width (e.g., Horne 1986). To flux calibrate the spectra, the single-mask extracted 1D spectra are convolved with the broad/medium-band filters, and then we compare to the total photometry (Weaver et al. 2024), and model the wavelength-dependent linear correction with a first-order polynomial. Reduced data will be presented in S. H. Price et al. (2024, in preparation).

2.3. Gravitational Magnification

Throughout this study we use the latest version (`v1.1`) of the Furtak et al. (2023c) strong lensing model of A2744.[35] The parametric strong lensing model was constructed with an updated version of the Zitrin et al. (2015) parametric method (Pascale et al. 2022; Furtak et al. 2023c) and includes 421 cluster member galaxies and five smooth cluster-scale dark matter halos. The `v1.1` has been updated with five new multiple image systems and additional spectroscopic redshifts (Bergamini et al. 2023), and is thus constrained with 141 multiple images belonging to 48 sources across the several main clumps of the cluster. The final lens plane image reproduction error is $\Delta_{\rm rms} = 0\farcs51$. We compute magnifications and their uncertainties for our sample at each object's position and spectroscopic redshift.

3. Photometric and Spectroscopic Sample

First, we briefly review the basic properties of the photometrically selected AGN sample (Section 3.1; L23), then we summarize the objects targeted for MSA/PRISM spectroscopy.

3.1. Sample of Red Compact Sources

We build the photometric sample of AGN candidates in a number of key steps. First we select compact and red sources, with the following color and morphology cuts. With a signal-to-noise ratio (S/N) in F444W > 14 and $m_{\rm F444W} < 27.7$ mag within a $0\farcs32$ aperture, we select sources that are (red1 |red2) and compact, where

$$\begin{aligned}\text{red1} = &(\text{F115W} - \text{F150W} < 0.8) \wedge \\ &(\text{F200W} - \text{F277W} > 0.7) \wedge \\ &(\text{F200W} - \text{F356W} > 1.0),\end{aligned}$$

$$\begin{aligned}\text{red2} = &(\text{F150W} - \text{F200W} < 0.8) \wedge \\ &(\text{F277W} - \text{F356W} > 0.7) \wedge \\ &(\text{F277W} - \text{F444W} > 1.0),\end{aligned}$$

and

$$\text{compact} = f_{\rm F444W}(0\farcs4)/f_{\rm F444W}(0\farcs2) < 1.7,$$

for $f_{\rm F444W}(0\farcs4)$ measured within a $0\farcs4$ diameter aperture. This initial sample comprises 40 sources, the "compact red" sample. We show the full selection in Figure 1; the main difference between red1 and red2 is that red2 favors higher-redshift galaxies owing to the redder filters used. The red2 sample accounts for 58% of the photometric sample and has been the focus for spectroscopic follow up, representing 82% of our spectroscopic targets.

For context, the L23 color criteria, specifically red2, used to select the compact red sample are similar to those used by Labbé et al. (2023b) to select "v-shaped" SEDs as candidates for massive galaxies at similar epochs, but with an important distinction. The red2 criteria consist of a more stringent set of cuts to ensure that the sources are point-source dominated and show two red consecutive colors in the long-wavelength (LW) NIRCam filters, thus favoring sources with red continuum slopes rather than contributions from emission lines or a continuum break. The overlap between the samples is discussed in Section 5.

As a final step, L23 identified a "clean" sample of 17 objects keeping only sources where two-dimensional image fitting in F356W indicated <50% of the light residing in an extended component and where SED fitting indicated the broadband SEDs could not be fit without an AGN component.

In nearly all cases, the highest-priority targets are those with deep ALMA limits, because in these cases we can effectively rule out dusty star formation as the origin of the red continuum,

[34] Available from doi:10.17909/8k5c-xr27.

[35] The `v1.1` lensing maps are publicly available at https://jwst-uncover.github.io/DR1.html#LensingMaps.

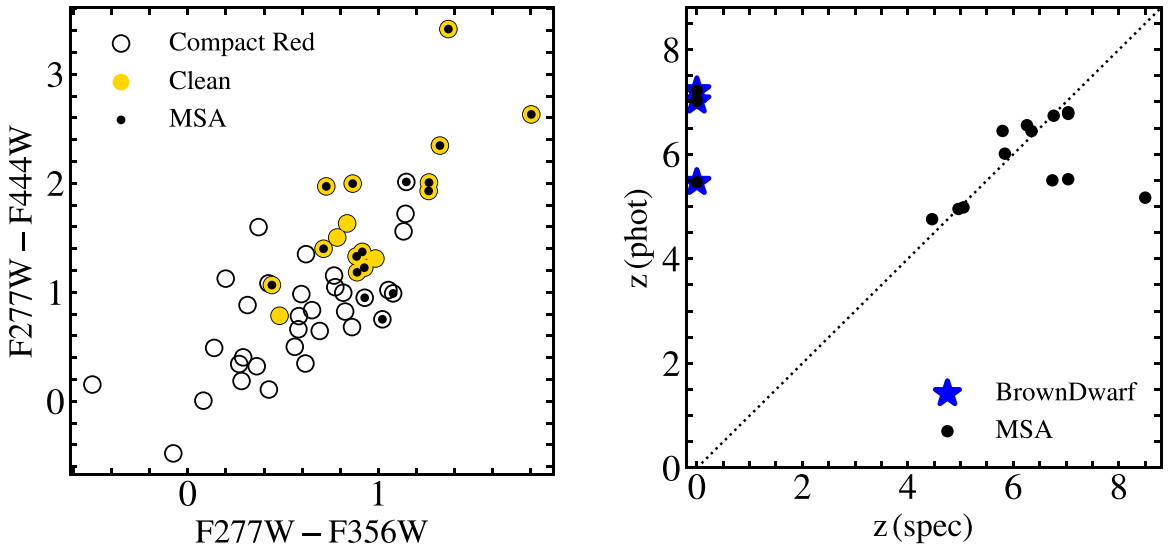

Figure 1. Left: the primary color–color selection used to select the compact red sources. We show the full sample of 40 compact red sources (open circles), the 17 clean targets (yellow), and the spectroscopically targeted sources (black dots are those observed with the MSA). Comparison of the photometric redshifts measured from the NIRCam photometry using custom templates from L23, as compared with the spectroscopic redshifts. The brown dwarfs are indicated with stars.

Table 1
Sample

MSAID (1)	R.A. (2)	Decl. (3)	z_{spec} (4)	μ (5)	μ_{low} (6)	μ_{high} (7)	F444W (8)	F277 – F444 (9)	F277 – F356 (10)	Flg (11)	MSA (12)	T_{exp} (13)
2008	3.592423	−30.432828	6.74	1.69	1.68	1.72	27.3	1.39	1.06	0	1	2.7
4286	3.619202	−30.423270	5.84	1.62	1.61	1.64	24.8	2.03	1.19	0	2	2.7
10686	3.550838	−30.406598	5.05	1.44	1.45	1.47	24.3	1.05	0.49	1	1	2.7
13123[a]	3.579829	−30.401570	7.04	6.15	5.96	6.69	25.0	2.66	1.89	1	2, 3, 5, 6, 7	17.4
13821	3.620607	−30.399951	6.34	1.59	1.57	1.61	25.0	2.33	1.40	1	1	2.7
15383[a]	3.583534	−30.396678	7.04	7.29	5.78	7.30	25.3	2.45	1.71	1	2, 3, 6	9.9
16594[a]	3.597203	−30.394330	7.04	3.55	3.38	3.70	26.3	1.97	1.26	1	1, 5, 6, 7	14.7
20466	3.640409	−30.386437	8.50	1.33	1.31	1.34	26.2	1.92	0.72	1	2	2.7
23608	3.542815	−30.380646	5.80	2.07	2.07	2.13	24.9	0.79	0.88	0	3	2.7
28876	3.569596	−30.373222	7.04	2.70	2.60	2.73	26.8	2.10	1.49	1	1, 4	6.4
32265	3.537530	−30.370168	...	⋯	⋯	⋯	27.3	0.97	0.68	1	3, 5, 6, 7	14.7
33437	3.546419	−30.366245	...	⋯	⋯	⋯	27.0	2.06	0.97	1	3, 5, 6, 7	14.7
35488	3.578984	−30.362598	6.26	3.38	3.14	3.74	24.5	0.83	0.99	0	1	2.7
38108	3.530009	−30.358013	4.96	1.59	1.58	1.62	24.7	1.06	0.83	1	4	3.7
39243	3.513894	−30.356024	...	⋯	⋯	⋯	25.6	3.63	1.53	1	4	3.7
41225	3.533994	−30.353308	6.76	1.50	1.49	1.53	25.9	1.13	0.71	1	4	3.7
45924	3.584758	−30.343630	4.46	1.59	1.58	1.65	22.1	0.54	0.94	1	4, 5, 6, 7	15.7

Note. Table of objects that satisfy (red1|red2) and compact. Column (1): MSA ID. Column (2): R.A. Column (3): decl. Column (4): spectroscopic redshift. Column (5): total magnification (μ) based on the `v1.1` UNCOVER strong lensing model (see Section 2.3). Column (6): magnification 68% low value. Column (7): magnification 68% high value. Column (8): F444W mag. Column (9): F277W – F444W color (mag). Column (10): F277W – F356W color (mag). Column (11): flag for the high-priority photometric sample. Column (12): MSA number (1–7). Column (13): total exposure time (h).
[a] The three images of the multiply imaged red AGN presented in Furtak et al. (2023a, 2023b).

unless we were to invoke much hotter dust than is seen at these (or any) redshift. However, only 3/20 targets with ALMA coverage favored SED solutions without an AGN component, so we will assume that the NIRCam color-selected sample is largely representative of the SED-selected sample. We will discuss the AGN yield under different cuts in Section 5.

3.2. Spectroscopic Sample

In designing the MSA PRISM masks, we prioritized observing the compact red sources from L23. We obtained spectra for most (75%) of the highest-priority targets, as is shown in Figure 1 (see also Table 1).

4. Spectral Analysis

We targeted with the NIRSpec/PRISM 17 sources that were photometrically identified in the UNCOVER photometry (L23). Of these, 14 are extragalactic sources and three turn out to be cool brown dwarfs (Burgasser et al. 2024). Three of the extragalactic sources are confirmed as multiply lensed images of the same source, A2744-QSO1 (Furtak et al. 2023a, 2023b), leaving 12 unique nonstellar sources. All have redshifts $4.5 < z_{spec} < 8.5$. Overall the photometric redshifts were accurate (Figure 1), with a median offset in $\delta z/(1+z)$ of $\langle z \rangle = 0.008$ and $\sigma_{MAD} = 0.03$, but for some objects the redshift was underestimated (e.g., Kokorev et al. 2023), due to

degeneracy between redshifts where [O III] or Hα are in the F410M or F444W bands.

The main goal of this paper is to determine the nature of these sources. Based on their unique properties—detected UV continuum, red optical continuum, undetected by ALMA, and spatially compact—we proposed, based on SED fitting, that the sources are likely to be AGN. We now ask whether the spectra provide evidence for an accreting black hole. The main evidence we will present is in the form of broad Balmer lines, which have long been an accepted signature of gas orbiting a central black hole in a broad-line region (e.g., Osterbrock 1977).

4.1. Line Fitting

From our broad wavelength coverage, from 1 to 5 μm, we cover from Lyα to Balmer lines at $4.5 < z < 8.5$. The spectra are very rich, albeit at relatively low ($R = 100$–500) dispersion. In this section, we will focus only on fitting the strong optical emission lines Hβ, [O III] λλ4959, 5007, Hα, and [N II] λλ6584, 6548. Note that because Hα falls at the reddest end of the spectrum, we have enough spectral resolution to model the [N II] lines separately from Hα.

In all cases we model the narrow forbidden lines with a single velocity width, and the ratios of the [O III] and [N II] doublets are fixed to ∼3. We model the continuum as a power law, normalized at 5100 Å. We then perform two different fits to the Hβ + [O III] + Hα + [N II] complex. In all fits, the radial velocities of all lines are tied together. First, we perform a narrow-line-only fit, where all the lines are fixed to the same velocity width, with a flat broad prior on the width up to 800 km s $^{-1}$. Then we perform a two-component fit with narrow and broad components to the Balmer lines. In this fit, all narrow lines are fixed in velocity width and fit over a narrow prior range (50–150 km s^{-1}). The ratio of narrow Hα/Hβ flux is fit over a prior range of 3–20 ($A_V \sim 0$–5) under the assumption of case B recombination (Osterbrock 1989). Broad Hβ and Hα fluxes are fitted independently, and the width of Hα is constrained to fall within a factor of 2 of Hβ. In the first fit we constrain eight free parameters (including a power-law continuum) and in the second model we add four additional free parameters.

Each model is then forward modeled through the instrument before calculating the likelihood. We use the predicted prelaunch instrumental broadening from JDOX (Jakobsen et al. 2022), but because our targets are by definition point sources, the resolution is considerably better than the nominal resolution for a uniformly illuminated slit (by up to a factor 2; de Graaff et al. 2023). On the other hand, the rectification and combination of the spectra results in additional broadening due to the relatively large pixel size compared to the instrument point-spread function. We therefore increase the nominal resolution by a conservative, uniform factor of 1.3, but caution that we then neglect any wavelength dependence of the correction factor on the line-spread function. The effect on the inferred broad-line widths is negligible, but the inferred widths for the narrow-line components suffer from a systematic uncertainty. For the fitting, we define a variable wavelength grid that oversamples the native resolution by a factor of 4, convolve the model with the instrumental broadening, and then resample onto the wavelength grid while preserving the flux.

The full set of narrow-only and two-component fits are presented in Figures 2 and 3, the continuum fits are presented in Table 2, and the broad Hα parameters are presented in Table 3. To explore the impact of the degeneracy between the broad and narrow lines, we perform an additional two-component fit in which we fix the Balmer decrement to fall between Hα/Hβ = 4–6, corresponding to the continuum-derived $A_V \approx$ 1.5 mag as is seen in our more conservative continuum fits (Section 4.4). We find that in all cases but one, the derived Hα width agrees within 5%–10% of our fiducial fits. In the case of MSAID23608, which has a very strong narrow-line component, the broad Hα width decreases to 1500 km s^{-1}. Thus, we are confident that overall, our broad-line widths are robust to degeneracy with the narrow components.

4.2. Identifying Broad Balmer Lines

Two targets (A2744-QSO1 and MSAID20466) have previously been identified as robust broad-line AGN (Furtak et al. 2023b; Kokorev et al. 2023). We here examine the remaining 10 objects, after removing the three brown dwarfs. The majority of our targets are at $z < 7$, meaning that Hα falls fully in the spectrum. Given the significant dust reddening, we focus exclusively on identifying broad Hα, since given the typical Balmer decrements ∼ 5–10, we have a substantially higher S/N in Hα than Hβ.

To determine which sources have broad lines, we apply the following three criteria. First, we insist that the fit improvement in χ^2 be better than 3σ ($\Delta\chi^2 > 11.5$ for four additional degrees of freedom) between the narrow-only and two-component fits (MSAID2008 and MSAID35488 are removed at this step). Second, we require that the two-component broad Hα have a FWHM > 2000 km s^{-1}. We choose 2000 km s^{-1} as a conservative limit, compared to the bimodality at 1200 km s^{-1} identified by Hao et al. (2005). Finally, we remove any object with a $<5\sigma$ detection of a broad line, where σ is measured as the 68% distribution from the nested sampling (MSAID10686 is removed at this step). All objects have $>5\sigma$ narrow [O III] and Hα detections. The "unconfirmed black hole" targets could show evidence of broad emission lines with higher spectral resolution (and in one case complete coverage of Hα). Specifically, many very significant but weak broad lines have been identified in higher-resolution JWST spectroscopy (e.g., Harikane et al. 2023; Larson et al. 2023; Maiolino et al. 2023). We could not identify such lines in our data, and so we retain a label of "unconfirmed" for the remaining three objects. We do not report broad-line fluxes or black hole masses for the unconfirmed targets.

Another question is whether the broad lines might arise from outflows, rather than the broad-line region of the AGN. It is true that outflows ∼2000 km s^{-1} have been seen in narrow permitted and forbidden lines in very luminous (and reddened) AGN at $z \sim 2$ (e.g., Zakamska et al. 2016). However, while we do not have robust measurements of the narrow-line widths, we know that they are <500 km s^{-1}, so that the broad permitted lines almost certainly arise from the broad-line region.

4.3. Other Emission Lines

We do not present exhaustive fits of other UV emission lines in this work. However, we did perform a search for the forbidden line [Ne V] λ3426. This line is widely accepted as a likely indicator of AGN activity, given its ionization potential of 95 eV, although it has also been attributed to Wolf–Rayet stars and/or shocks in various situations (e.g., Abel & Satyapal 2008; Izotov et al. 2012; Leung et al. 2021). We only find compelling evidence for [Ne V]

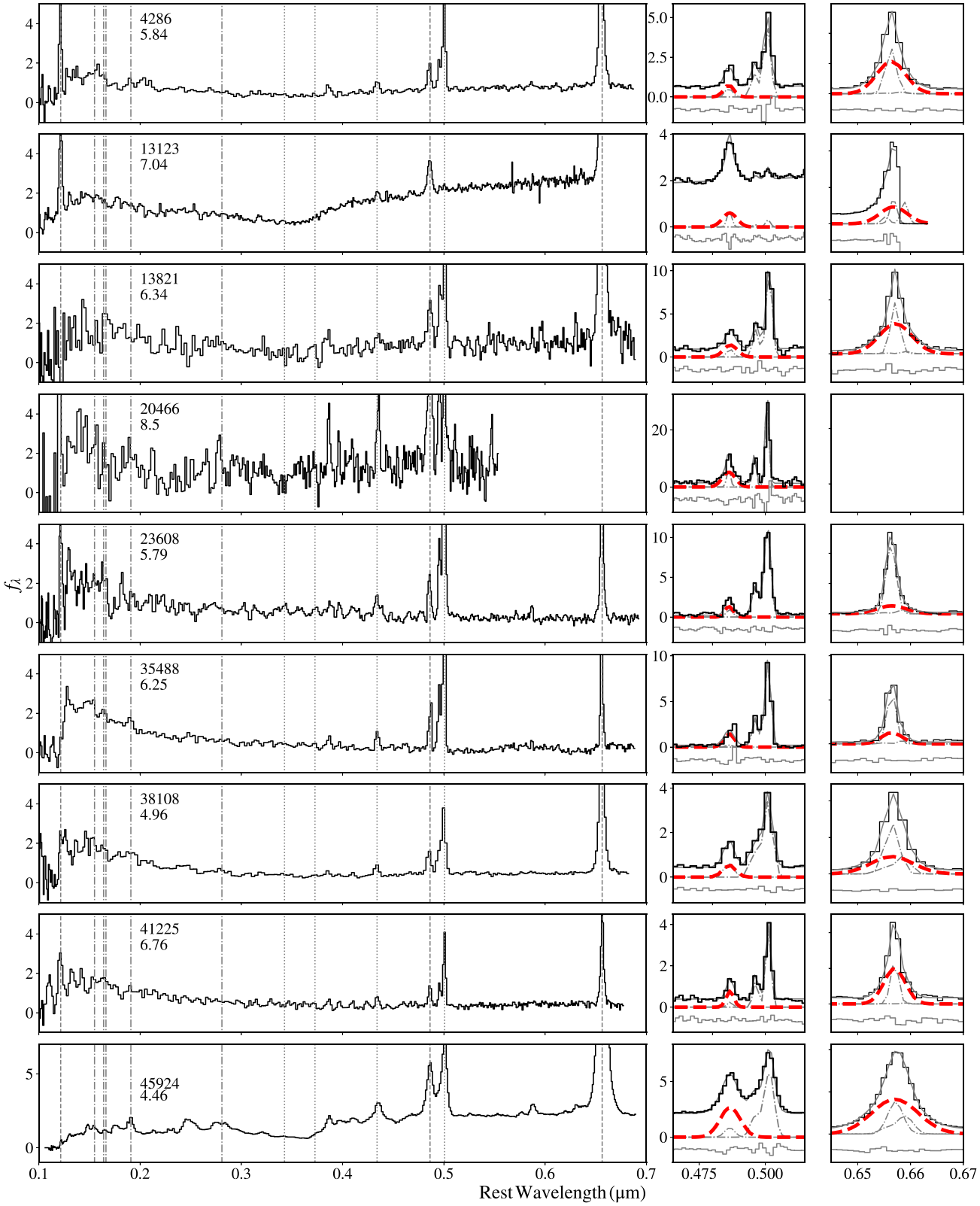

Figure 2. Left: NIRSpec/PRISM spectra of the nine confirmed broad-line AGN in the sample. Spectra are plotted in rest-frame wavelength and have been normalized at 2500 Å. The vertical lines indicate the rest-fame wavelengths of the hydrogen lines (Lyα, Hβ, and Hα) as dashed lines, broad permitted metal lines (C IV λ1550, He II λ1640, O III] λ1663, C III] λ1909, and Mg II λ2800) as dashed–dotted lines, and forbidden lines ([Ne V] λ3426, [O III] λ3727, [O III] λ4363 [note this is blended with Hγ], and [O III] λ5007) as dotted lines. In the case of MSAID13123, we are actually plotting the coadded spectrum across all three images from Furtak et al. (2023b). Middle: Fits to the Hβ + [O III] spectral region. We show the data (black histogram), the full model (gray solid), the narrow-line fits (dotted–dashed), and the broad-line fits (thick red dashed). Right: Fits to the Hα + [N II] region, where lines are the same as in the Hβ region. We only require a significant [N II] component in a couple of cases.

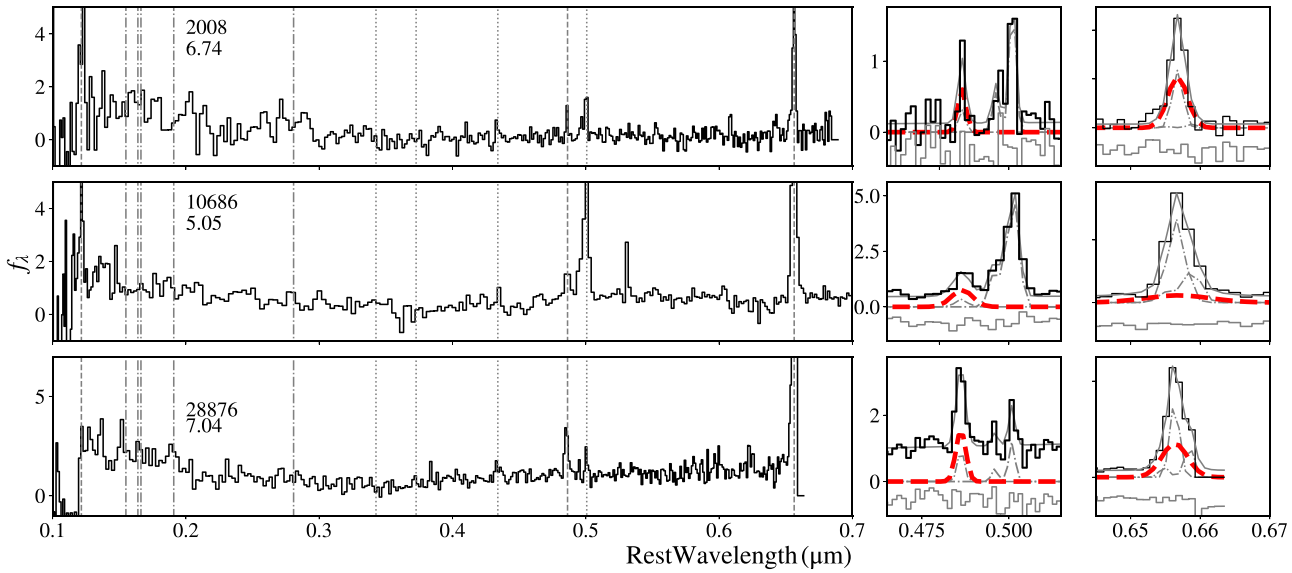

Figure 3. Left: NIRSpec/PRISM spectra of the unconfirmed broad-line AGN in the sample. Spectra are plotted in the rest frame and have been normalized at 2500 Å. The vertical lines indicate the rest-frame wavelengths of the hydrogen lines (Lyα, Hβ, and Hα) as dashed lines, broad permitted metal lines (C IV λ1550, He II λ1640, O III] λ1663, C III] λ1909, and Mg II λ2800) as dashed–dotted lines, and forbidden lines ([O III] λ3727, [O III] λ4363 [note this is blended with Hγ], and [O III] λ5007) as dotted lines. Middle: Fits to the Hβ + [O III] spectral region. We show the data (black histogram), the full model (gray solid), the narrow-line fits (dotted–dashed), and the broad-line fits (thick red dashed). Right: Fits to the Hα + [N II] region, where the lines are the same as in the Hβ region. Note that in the case of MSAID13123, the redshift of $z = 7.04$ truncates the Hα line

Table 2
Continuum Fits

MSAID (1)	$\alpha_{\rm opt}$ (2)	$\beta_{\rm UV}$ (3)	$A_{V,\ 0.45}$ (4)	$A_{V,\ \rm fit}$ (5)	$L_{5100,c}$ (6)	$L_{5100,{\rm H}\alpha}$ (7)
2008	1.4 ± 0.3	-1.9 ± 0.3	2.1 ± 0.5	2.4 ± 3.0	43.5	43.7
4286	0.9 ± 0.1	-1.6 ± 0.1	1.3 ± 0.2	2.7 ± 0.2	44.6	44.7
10686	0.4 ± 0.3	-1.6 ± 0.1	2.0 ± 1.1	3.2 ± 0.2	44.9	44.3
13123[a]	1.2 ± 0.3	-1.4 ± 0.1	3 ± 0.5	⋯	44.4	43.8
13821	1.0 ± 0.3	-1.2 ± 0.1	1.1 ± 0.3	1.7 ± 0.2	44.2	44.5
20466[b]	0.5 ± 0.3	-0.7 ± 0.2	$2.1^{+1.1}_{-1}$	1.9 ± 0.2	44.5	44.9
23608	0.0 ± 0.1	-1.5 ± 0.1	0.1 ± 0.1	1.9 ± 0.7	43.5	43.5
28876	1.0 ± 0.2	-2.1 ± 0.1	1.4 ± 0.1	2.9 ± 1.2	44.1	43.9
35488	0.1 ± 0.2	-2.3 ± 0.1	0.3 ± 0.5	2.0 ± 0.3	44.2	44.1
38108	0.5 ± 0.1	-1.9 ± 0.1	0.8 ± 0.2	3.3 ± 0.2	44.7	44.7
41225	0.3 ± 0.1	-1.7 ± 0.1	1.0 ± 0.2	3.9 ± 0.1	45.0	44.7
45924	0.5 ± 0.1	0.0 ± 0.1	1.6 ± 0.3	1.1 ± 0.9	44.9	45.3

Notes. Table of continuum measurements from the PRISM spectroscopy.
[a] The highest S/N spectrum of the triply imaged object from Furtak et al. (2023b). The A_V is derived from the Balmer decrement for this source.
[b] The $z = 8.5$ broad-line AGN discussed by Kokorev et al. (2023). In this case the A_V measurements are derived from the Balmer decrement and a full spectral fit, while L_{5100} in column (7) is derived from Hβ assuming a ratio of Hα/H $\beta = 3.5$. Column (1): MSA ID. Column (2): optical slope $f_\lambda \propto \lambda^\alpha$, fitted redward of 4400 Å. Column (3): UV slope $f_\lambda \propto \lambda^\beta$, fitted blueward of 3000 Å. Column (4): A_V (mag) estimated from the continuum slope assuming an intrinsic AGN power-law slope of $\alpha_{\rm opt} = 0.45$ and an SMC reddening law. Column (5): A_V (mag) estimated from the continuum slope assuming an intrinsic AGN power-law slope as fitted to the UV component of the spectrum and an SMC reddening law. Column (6): demagnified and dereddened luminosity at 5100 Å (units of erg s^{-1}) as estimated from the measured continuum and the A_V from column (5). Column (7): demagnified and dereddened luminosity at 5100 Å (units of erg s^{-1}) as estimated from the measured Hα luminosity and the A_V from column (5).

in source 45924, which is already a very strong AGN candidate by virtue of its broad line width of FWHM(Hα) = 4000 km s^{-1}. Since [Ne V] is typically 0.02–0.2 the strength of [O III], and considering the strong reddening, this nondetection is not surprising (Netzer 1990). We also attempt to decompose the [O III] λ4363 and Hγ emission lines, which may also provide corroborating evidence for excitation by an AGN (Baskin & Laor 2005; Binette et al. 2022). However, given our spectral resolution, we do not achieve robust decompositions for any of the unconfirmed AGN candidates.

4.4. Balmer Decrement and Continuum Slopes

By selection, our targets contain steep red continua. With the spectra, we have good constraints on both the UV and optical slopes, which we denote as $\beta_{\rm UV}$, $f_\lambda \propto \lambda^\beta$ ($\lambda < 3000$ Å) and $\alpha_{\rm opt}$, $f_\lambda \propto \lambda^\alpha$ ($\lambda > 4000$ Å). For the definitive and unconfirmed broad-line sources, we find $\langle\beta_{\rm UV}\rangle = -1.5 \pm 0.7$ and $\langle\beta_{\rm UV}\rangle = -1.9 \pm 0.2$, respectively. The unconfirmed AGN candidates are bluer in the rest-frame UV than the average AGN in our sample, but all the targets are on the redder end of what is seen

for F444W-selected galaxies with $4 < z < 7$ (Bouwens et al. 2016; Bhatawdekar & Conselice 2021; Nanayakkara et al. 2023; Topping et al. 2023). The optical slopes are by construction quite red, with $\langle \alpha_{\rm opt} \rangle = 0.5 \pm 0.3$ and $\langle \alpha_{\rm opt} \rangle = 0.9 \pm 0.4$ for the AGN and unconfirmed samples, respectively (Table 2).

We now try to estimate the dust reddening. Nominally, we measure the Balmer decrement from the narrow Balmer line fits (ranging from 4 to 15), implying $A_V \sim 1$–5. Because of the degeneracy with the broad Balmer lines, the Balmer decrements are not well constrained in general. Small changes in the broad-line fits can lead to large fluctuations in the Balmer decrements. Note that we do not trust broad-line Balmer decrements, since self-absorption in the broad-line region can also change the Hα to Hβ ratio (Korista & Goad 2004). We thus base our reddening estimates on the continuum slopes.

We fit the UV and optical sides of the spectra separately to derive $\beta_{\rm UV}$ and $\alpha_{\rm opt}$ as power laws in f_λ. To derive the dust reddening, we must assume an intrinsic (unreddened) spectral shape. All of our determinations of A_V are under the assumption that the red continuum is dominated by AGN light (see Section 6). We take two AGN models. First, we use the Sloan Digital Sky Survey (SDSS; Yorket al. 2000) composite AGN templates from Vanden Berk et al. (2001). The composite slope has $\beta_{\rm UV} = -1.5$ in the UV. The UV slope of the SDSS template is consistent with many other works (e.g., Davis et al. 2007), and seems to hold over a wide range of redshift (Temple et al. 2021). The SDSS template then has a break to $\alpha_{\rm opt} = 0.45$ in the rest-frame optical at $\lambda \gtrsim 4000$ Å. The redder slope could be an intrinsic spectral change, or the impact of galaxy light redward of the 4000 Å break, which is hard to determine robustly. Hence, we fit the SDSS-QSO template independently to each spectrum in the range $\lambda < 3500$ Å and $\lambda > 4300$ Å (to avoid the observed break seen in several of the spectra). In each case we allow a free extinction parameter characterized by the SMC reddening curve (Gordon et al. 2003).

We also perform a second more agnostic fit in which we fit the rest-frame UV slope directly assuming $F_\lambda \propto \lambda^\beta$, and then assume this empirical slope holds over the full spectral range. In the case that the UV emission arises from scattered light, a single spectral slope should describe the scattered and intrinsic slopes. We allow for an additional two free parameters, an A_V affecting an SMC-like reddened F_λ component to describe the red end of the spectra, and a zero-reddening scattered light fraction ($f_{\rm scatt}$) that describes the rest-frame UV portion of the final model such that $f_{\lambda,\rm model} = f_{\rm scatt} F_{\lambda,\rm UV}$.

The reddening derived from the SDSS template is tabulated as $A_{V,0.45}$ due to the rest-frame optical slope of the composite spectrum. The agnostic empirical fit is denoted as $A_{V,\ \rm fit}$ because we fit directly for β. These two reddening values thus bracket a reasonable range of reddening levels, and are presented in Table 2.

We find that although the flux level in the UV is suppressed compared to the standard AGN template, the UV slopes are very similar to the unreddened UV slope of the SDSS AGN template ($\langle \beta_{\rm UV} \rangle = -1.5 \pm 0.7$). The rest-frame optical slopes are more variable. In Section 6.1, we will discuss the origin of the UV emission.

5. High Fraction of AGN in Red Photometric Samples

Our NIRSpec/PRISM spectra confirm the AGN hypothesis for a majority of the objects photometrically selected in L23. With the spectra in hand, we can explore the demographics of red sources at high redshift, as well as devise refined photometric selection criteria for future searches.

5.1. Yield and Contaminants

Of the 17 targets from L23 with UNCOVER PRISM spectra, 11 have unambiguous evidence for broad emission lines, including three which are multiple images of the same target (Furtak et al. 2023b). Three targets do not show clear evidence for broad emission lines, and a further three are brown dwarfs (Burgasser et al. 2024). Therefore $11/17 = 65\%$ of the sample are confirmed as broad-line AGN. Accounting for the multiply lensed source, the confirmed AGN fraction among the targeted extragalactic objects in our sample is $9/12 = 75\%$. This is only the fraction of AGN for the specific color and compactness criteria we applied (see more details in Section 5.2), not the full galaxy population.

One obvious contaminant is brown dwarf stars. A simple color cut, excluding all sources bluer than F115W − F200W < -0.5 (blue box in Figure 4), would remove the majority of brown dwarfs from high-z galaxy selections in high-latitude deep fields (see also Langeroodi & Hjorth 2023). Based on the simulations from Burgasser et al. (2024) in the UNCOVER area we expect ∼5 low-metallicity halo brown dwarfs, expected to have the bluest F150W − F200W colors (see Figure 4). Some contaminants at redder colors would remain: ∼2 metal-rich brown dwarfs that reside in the Galactic thin disk are expected. The higher-metallicity brown dwarfs in the thin disk should be bright, F444 < 24 mag, since the limited vertical scale height of the disk will limit these brown dwarfs to be within a few hundred parsecs. A more refined filter could possibly be defined from a larger model and/or template sample. Upcoming medium-band data (GO-4111; PI: W. Suess) will allow for even cleaner identification of brown dwarfs (Hainline et al. 2023b).

5.2. Updated Photometric Selections of High-redshift Galaxies and AGN

Here we define updated NIRCam-only criteria to the selections of L23 and Labbé et al. (2023b). Specifically, we start with the same S/N(F444W) > 14 and $m_{\rm F444W} < 27.7$ mag cuts as before. Then, we define a "v-shape" color selection to mimic that of Labbé et al. (2023b), designed to find candidate massive high-redshift galaxies

$$v - \text{shape}$$
$$(-0.5 < \text{F115W} - \text{F200W} < 1.0) \wedge$$
$$(\text{F277W} - \text{F444W} > 1.0).$$

The main difference with respect to Labbé et al. (2023b) is using F115W – F200W rather than F150W – F200W, and a blue limit to facilitate removing brown dwarfs. In addition, since we lack deep Advanced Camera for Surveys (ACS) coverage, we forego the HST/ACS optical nondetection criterion, thereby extending the selection toward lower redshifts $z \sim 5$. This selection produces 31 unique sources in UNCOVER and is both effective and complete at identifying high-redshift galaxies with red rest-frame optical colors. The median $\langle z \rangle = 6.9 \pm 1.0$ and $28/31 = 90\%$ sources have $z_{\rm phot} > 5$ (see Figure 4). In total 15 sources were targeted with UNCOVER PRISM spectroscopy, 11 presented in this paper and a further four presented in S. H. Price et al. (2024, in preparation). All are at $4.5 < z < 8.5$. Only one source with

Table 3
Hα Fits

MSAID (1)	FWHM$_n$ (2)	FWHM$_{two}$ (3)	f_{two} (4)	χ^2_n (5)	χ^2_{two} (6)	$L_{H\alpha}$ (7)	M_{BH} (8)	L_{bol} (9)
2008	650 ± 100	1200 ± 430	1.4 ± 0.3	94	94	…	…	…
4286	800 ± 10	2900 ± 1040	13.7 ± 0.4	807	361	43.4	8.0 ± 0.3	45.4 ± 0.3
10686	60 ± 10	4900 ± 1570	5.5 ± 1.6	332	296	…	…	…
13123[a]	…	2670 ± 170	5.0 ± 0.45	…	…	42.7	7.3 ± 0.2	45.0 ± 0.1
13821	790 ± 10	3100 ± 710	17.4 ± 0.8	461	248	43.3	8.1 ± 0.2	45.4 ± 0.2
20466[b]	203 ± 154	3439 ± 413	2.3 ± 0.2	4817	410	43.8	8.17 ± 0.42	$45.8^{+0.3}_{-0.1}$
23608	70 ± 10	2900 ± 340	2.4 ± 0.2	409	341	42.3	7.5 ± 0.2	44.2 ± 0.4
28876	650 ± 70	1800 ± 650	2.2 ± 0.4	265	265	…	…	…
35488	90 ± 10	1900 ± 210	10.9 ± 2.1	1123	976	42.8	7.4 ± 0.2	44.8 ± 0.4
38108	800 ± 10	4100 ± 1980	14.3 ± 0.5	671	215	43.4	8.4 ± 0.5	45.3 ± 0.5
41225	510 ± 30	2000 ± 600	4.7 ± 0.3	539	435	43.5	7.7 ± 0.4	45.3 ± 0.5
45924	70 ± 10	4500 ± 40	383.4 ± 0.4	1621505	90681	44.0	8.9 ± 0.1	46.4 ± 0.2

Note. Table of Hα measurements from the PRISM spectroscopy. *a* is the highest S/N spectrum of the triply imaged object from Furtak et al. (2023b), while *b* is the $z = 8.5$ broad-line AGN from Kokorev et al. (2023). Column (1): MSA ID. Column (2): FWHM(Hα), narrow-only fit (units of km s^{-1}). Column (3): FWHM(Hα), two-component broad fit (units of km s^{-1}). (b) is measured from Hβ (Kokorev et al. 2023). Column (4): observed Hα flux, two-component broad fit (units of 10^{-18} erg s^{-1} cm^{-2}). (b) is measured from Hβ (Kokorev et al. 2023). Column (5): χ^2 (narrow only). Column (6): χ^2 (two component). Column (7): demagnified and dereddened Hα luminosity (units of erg s^{-1}), using $A_{V,fit}$ from Table 2. Only definite broad-line objects have Hα luminosities listed. Column (8): black hole mass, using Hα line width and luminosity. The errors account for the line width errors and two reddening values. Some sources may not have an M_{BH} listed. Column (9): logarithm of the bolometric luminosity (units of erg s^{-1}), estimated from the Hα luminosity. The errors account for the two reddening values and the uncertainty in the bolometric correction.

F277W − F444W > 1 at $z > 5$ does not satisfy the v-shape selection.

Remarkably, with this color selection alone, at least 29% of the objects are spectroscopically identified AGN, corresponding to about one-third of all F277W − F444W > 1 at $z > 5$. We expect there are many inactive galaxies in the sample as well. Most of the Labbé et al. (2023b) objects found in the CEERS field are spatially resolved in the rest-frame UV, with densities similar to the cores of present-day ellipticals (Baggen et al. 2023). Out of four galaxies with spectroscopy in that sample, one was found to be a red broad-line AGN (Kocevski et al. 2023). Cycle 2 spectroscopy (program JWST-GO-4106, PI: E. Nelson) will determine what fraction of these color-selected but spatially resolved objects show evidence for AGN activity. We should emphasize that these red sources, be they galaxy or AGN powered, still constitute a small fraction of the galaxy population at this epoch; we will attempt to quantify the compact red AGN number density in Section 6.2.

To select red AGN more specifically in a similar fashion to the red2 selection of L23, we add an additional red color and compactness criterion compared to the v-shape criterion:

$$\text{compact red}$$
$$(-0.5 < \text{F115W} - \text{F200W} < 1.0) \wedge$$
$$(\text{F277W} - \text{F444W} > 1.0) \wedge$$
$$(\text{F277W} - \text{F356W} > 0.7) \wedge$$
$$\text{compact} = f_{\text{F444W}}(0\farcs4)/f_{\text{F444W}}(0\farcs2) < 1.5,$$

where the additional F277W − F356W > 0.7 facilitates selecting SEDs with red continuum slopes, rather than breaks or emission lines (Figure 4, top right), and the compactness criterion helps to target point-source-dominated sources (Figure 4, bottom left). These extra cuts remove roughly 50% of the v-shape targets. The main differences compared to L23 are the F115W − F200W > −0.5 brown dwarf removal and a slightly more stringent compact cut than in L23.

Among this more stringent AGN-focused selection, we find at least 75% are AGN. The AGN fraction is a function of F277W − F444W color (Figure 5). The majority of the broader sample of v-shape galaxies have 1 < F277W − F444W < 1.6. Therefore, an alternative high-yield selection of AGN can be made by selecting by F277W − F444W > 1.6. In this situation, >80% of the galaxies are AGN, while >90% of the compact red galaxies are AGN (see also Barro et al. 2023).

In short, among the $z > 5$ galaxies with red colors (−0.5 < F115W − F200W < 1.0 and F277W − F444W > 1), at least one-third are AGN. Making more stringent compactness and color criteria, or simply cutting at F277W − F444W > 1.6, can yield an 80%–90% AGN fraction.

6. The Nature of the "Little Red Dots"

Now focusing exclusively on the confirmed broad-line AGN, we explore their properties, including SEDs, luminosity functions, and black hole masses.

6.1. Origin of the Continuum

The compact red objects were photometrically selected not only to have a red continuum in the rest-frame optical, but also detectable UV emission. From a template fit to the photometry alone, we came to the conclusion that the red continuum was most likely dominated by reddened AGN light. With the spectra, we now ask whether it is possible to distinguish the origin of the rest-frame optical and UV continua more directly. We demonstrate the different methods of modeling the spectra with one example in Figure 6. We will defer full SED modeling to a future work, as that will require exploiting both the continua and the emission lines.

In the rest-frame optical, we immediately see that the observed red slopes are continuum dominated, not arising from high-equivalent width (EW) emission lines (see possibilities in Furtak et al. 2023a; Endsley et al. 2023). The rest-frame optical slopes are consistent with a reddened AGN template or dusty star formation, as was concluded from the photometric fitting. However, the broad emission lines provide an additional clue. We can calculate the

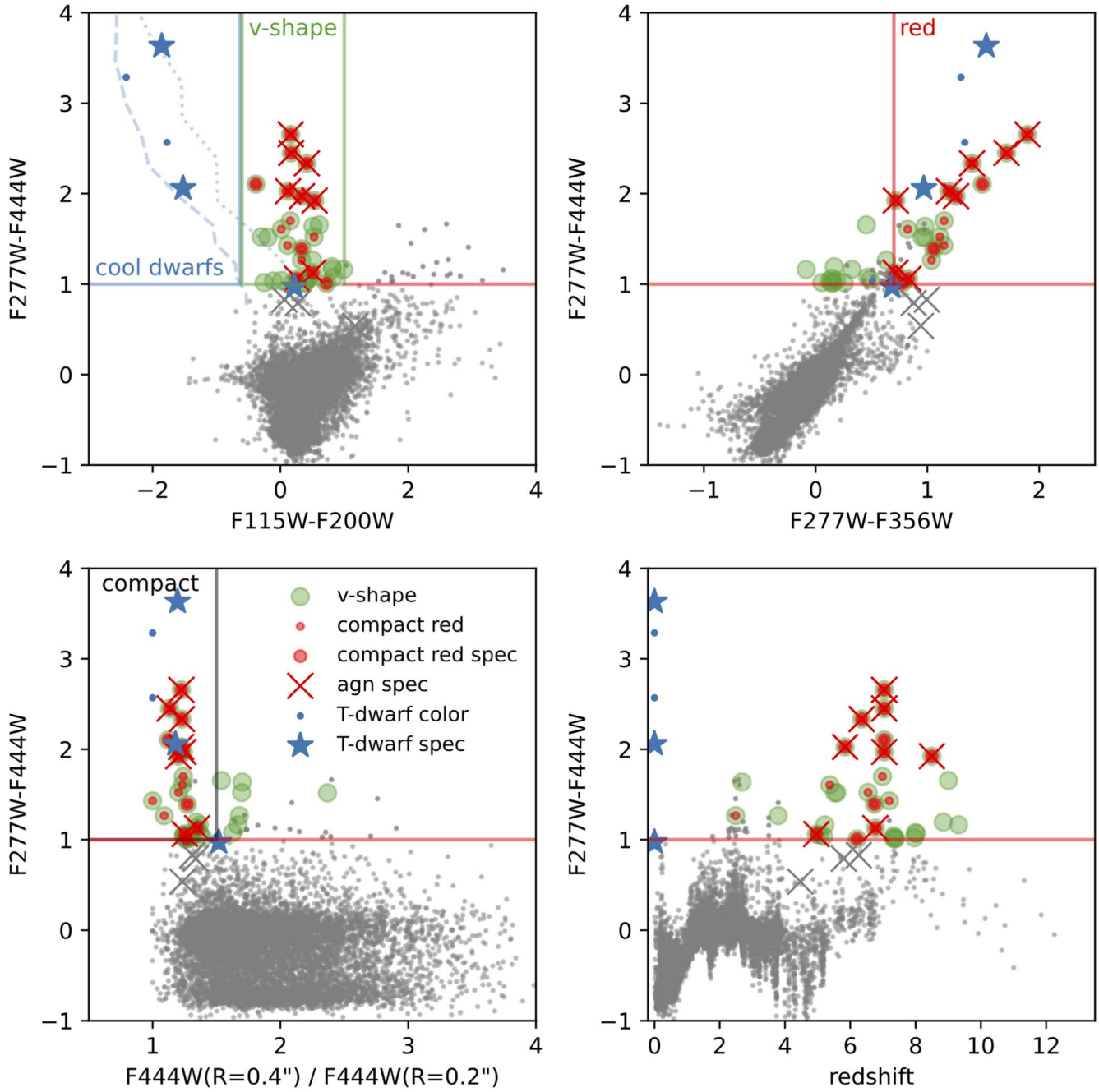

Figure 4. AGN in the context of high-redshift red galaxies. The gray points are the UNCOVER catalog for F444W > 27.7 mag and F444W S/N > 14. Top left: The NIRCam F115W − F200W vs. F277W − F444W bicolor selection identifies galaxies like those in Labbé et al. (2023b) that have a blue rest-frame UV continuum and red rest-frame optical continuum ("v-shape" SED). The AGN candidate sample of L23 is a subset of that (∼50%), selected to also have a red optical sloped continuum via a cut in two adjacent filters (top right), and compact size (bottom left), using a ratio of aperture fluxes as a proxy for size. Brown dwarf star contaminants generally have bluer F115W − F200W than galaxies and can therefore be isolated. Overplotted are synthetic color tracks from the LOWZ brown dwarf atmosphere models (Meisner et al. 2021) for $T_{\rm eff} \leqslant 1600$ K and solar [M/H] = 0 and −1.5. The v-shape criterion alone is very effective at selecting for $z > 5$ galaxies. A selection including the compact and red criterion is efficient at selecting red AGN.

expected continuum given the observed Hα luminosity (Greene & Ho 2005) and a measurement of reddening. We can also directly calculate the observed continuum. The two should match.[36] We include the two L_{5100} values, based on the continuum and Hα but using the same $A_{V,\rm fit}$, in Table 2. While the Hα-derived values tend to be a bit higher, they agree to within a factor of 2, suggesting that the broad Hα EWs are comparable to the low-redshift SDSS calibration sample from Greene & Ho (2005). The Hα EWs from pure star formation are much higher for dusty massive galaxies at lower redshift (Fumagalli et al. 2012; Whitaker et al. 2014). Given the detection of broad Hα and the AGN-like ratios of Hα to continuum, we conclude that the rest-frame optical is AGN dominated.

The dominant component from the AGN is the red continuum, and given the $A_V = 1$–3 that we infer, we could

[36] Comparing to the Greene & Ho (2005) relation is a bit easier than looking at the Hα EW distribution directly, since there may be subtle trends between line EWs and luminosities (e.g., Croom et al. 2002; Stern & Laor 2012) that are fitted for directly by Greene & Ho (2005).

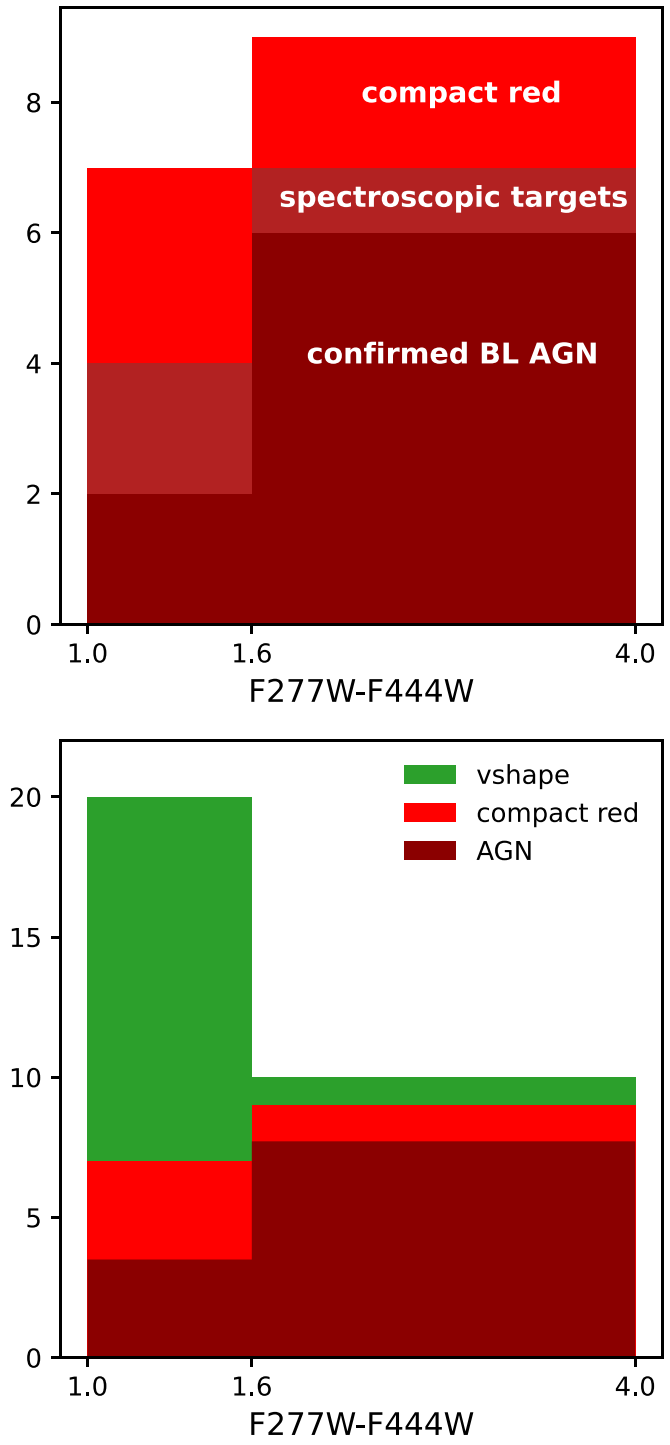

Figure 5. Distribution of object types as a function of F277W − F444W color. The top panel shows the compact and red NIRCam-selected sample, the number of spectroscopic targets, and the confirmed BL AGN. The bottom panel shows targets selected by the "v-shape" two-color cut (green), of which 90% are at $z = 5$–10, the number of compact and red-selected sources (red), and the estimated number of AGN (dark red).

not detect that component in the UV (see Figure 6). Instead, we must invoke a second component, which is brighter than the pure reddened AGN spectrum, but still only a few percent of an unreddened (blue) AGN. The two possible origins for this second UV-emitting component are either star formation from the host or some small fraction of the photons from the accretion disk, whether via scattering or direct leakage. Unfortunately, we cannot make a concrete determination of the origin of the UV based on the spectral slopes alone. The rest-frame UV slopes are quite consistent with the observed slopes of blue AGN with $A_V \approx 0$, and in some cases there are likely broad UV lines. With higher-resolution data this would be a smoking gun of AGN light dominating the UV. Alternatively, they could be consistent with the redder end of $4 < z < 7$ galaxies (e.g., Bouwens et al. 2016; Bhatawdekar & Conselice 2021), particularly those selected at F444W (e.g., Nanayakkara et al. 2023; Topping et al. 2023).

To explore the UV origin further, we can ask what UV luminosities we would expect given the intrinsic L_{5100} luminosities. We bracket the range of reasonable A_V using the two assumed intrinsic AGN slopes, and over that range we find that the observed L_{3000} is 1%–3% percent or 10%–20% of percent of the expected intrinsic L_{3000}, depending on whether we assume $\alpha_{\rm opt,\ intrinsic} = \beta_{\rm UV,measured}$ or $\alpha_{\rm opt,intrinsic} = 0.45$, respectively. The former can easily be explained by a scattered (or directly transmitted) AGN component, while 10%–20% fractions are likely too high for pure AGN scattering (e.g., Liu et al. 2009). In such cases, we would favor a star formation contribution to the UV. We choose not to fit the UV alone, since it has limited sensitivity to the stellar mass, but naively converting the M_{1450} measurements to star formation rates, and assuming that all the UV arises from star formation, we find average star formation rates of $\langle {\rm SFR} \rangle = 1.5\ M_\odot\ {\rm yr}^{-1}$. In terms of $L_{\rm H\alpha}$, we would expect 10–1000 times less Hα luminosity for this star formation rate than what we measure in the broad lines. On the other hand, this level of star formation seems both plausible and challenging to rule out from other measurements. In principle, the UV emission lines could distinguish the UV origins; higher-resolution data are needed for this purpose.

Overall, we conclude that the rest-frame optical continuum is dominated by a dusty broad-line AGN continuum, and that more work is needed to determine the origin of the UV emission definitively. Finally, we also note that two objects, MSAID45924 and the triply imaged A2744-QSO1 (MSAID13123 in this work), both have rather extraordinary spectral breaks that are not easily modeled with any AGN template. We leave to future work a more exhaustive fitting of their continua, to attempt to understand the nature of their extreme breaks.

6.2. Luminosity Functions

We now compute the rest-frame UV luminosity function of the red AGN at high-redshifts based on the spectroscopic sample alone. Since A2744 is a strong lensing field, the lensing distortion needs to be taken into account when computing the volume of each luminosity bin. To calculate the volumes, we follow the forward-modeling method used in the Hubble Frontier Fields by Atek et al. (2018): the sample completeness is assessed with a series of completeness simulations in which we populate the source plane with mock red AGN using the L23 SED, normalizing it to random UV luminosities and redshifts. These are then deflected into the lens plane with the deflection maps of the UNCOVER strong lensing model (see Section 2.3) and added into the mosaics on which we rerun the detection routines and assess the fraction of recovered sources to derive the selection function $f(z, M_{\rm UV})$. Note that the details of our completeness simulation methods will be published in I. Chemerynska et al. (2024, in preparation). The selection

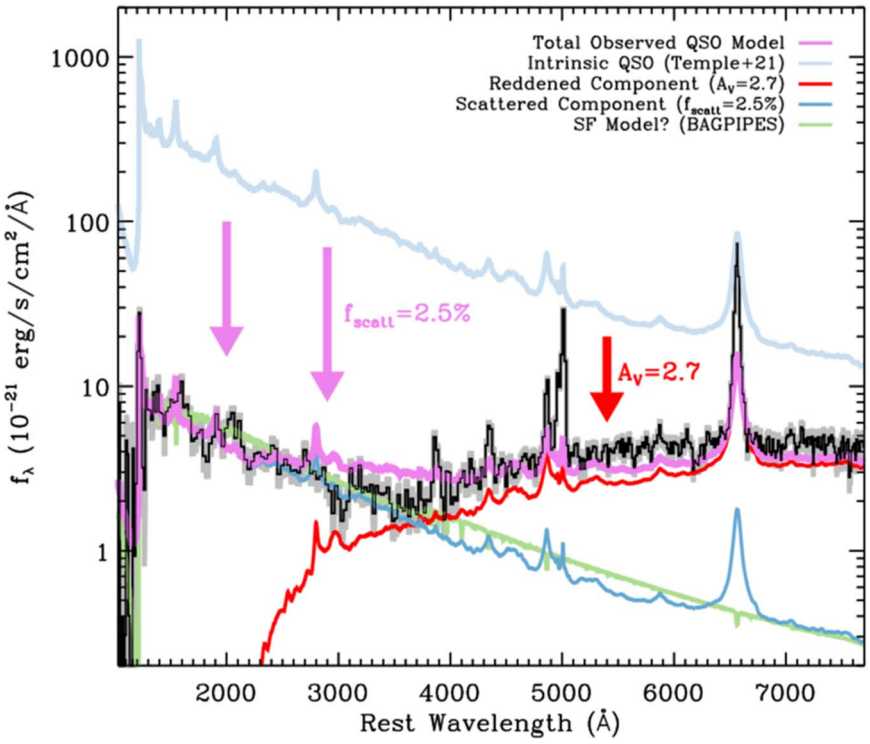

Figure 6. We illustrate our preferred model for the particular red and UV slopes seen in our objects using MSAID4286. The intrinsic AGN continuum (red) is highly reddened. Thus, the UV component cannot be explained by the primary AGN continuum. Here, we explore the possibility that the UV comes from scattered light, at 2.5% of the intrinsic UV (shown schematically in light blue). For illustration, we show here the Temple et al. (2021) template. However, we achieve even better fits when we use the observed UV slope as the intrinsic power-law AGN shape. We also overplot a stellar-population fit to the UV side of the spectrum with `Bagpipes` (Carnall et al. 2018, 2019), again to illustrate that with moderate star formation rates of a few solar masses per year, and $A_V \sim 0.6$ mag, it is possible to fit the UV continuum slope with starlight as well. The "?" indicates the uncertain contribution to the SED from star formation.

function is used to weight the comoving volume element, which is then integrated over the source plane area of sufficient magnification required to detect each object in all bands given the UNCOVER mosaic depths (see Equation (2) in Atek et al. 2018) to obtain the effective volume probed by UNCOVER. Note that since the UNCOVER source detection is performed in the stacked LW bands (see, e.g., Weaver et al. 2024) where the compact red objects are the brightest, our sample is complete down to $M_{\rm UV} \sim -16$ mag and objects brighter than $M_{\rm UV} \sim -17$ mag do not necessarily need to be magnified in order to be detected given the UNCOVER depths listed in Weaver et al. (2024). Our sample is binned in UV luminosity bins of 0.5 mag width. The number count uncertainties are derived by drawing 10^4 random luminosities from each object's $M_{\rm UV}$ error distribution and rebinning the luminosity function each time to allow objects to change luminosity bin. The uncertainty in magnification is taken into account in the computation of the UV luminosity uncertainties.

The resulting UV luminosity functions in the two redshift bins are presented in Table 4 and Figure 7. As established above, the spectroscopic sample represents a conservative but fairly accurate proxy for the true luminosity function of the reddened broad-line AGN. We confirm the result from L23 that the number densities of these red-selected AGN are higher by roughly 2 orders of magnitude compared to the UV-selected AGN at similar magnitudes. The number density we find is also comparable to what has been inferred for other moderate-luminosity red AGN samples at $z \approx 5$ (Barro et al. 2023; Kocevski et al. 2023; Matthee et al. 2023), and accounts for ~10%–20% of the general broad-line AGN population as selected with JWST (Harikane et al. 2023; Maiolino et al. 2023).

Table 4
Rest-frame UV Luminosity Functions of Our Sample of Red AGN

$M_{\rm UV}$	N	$\phi(M_{\rm UV})$ (Mpc^{-3} mag^{-1})
	$z \sim 5$–6 sample	
−19.5	3	$(3.0 \pm 0.6) \times 10^{-5}$
−19.0	2	$(2.1 \pm 0.7) \times 10^{-5}$
−18.5	2	$(2.1 \pm 0.8) \times 10^{-5}$
	$z \sim 7$–8 sample	
−19.0	1	$(1.3 \pm 0.5) \times 10^{-5}$
−18.0	2	$(2.6 \pm 0.7) \times 10^{-5}$
−17.0	2	$(4.0 \pm 1.0) \times 10^{-5}$

Note. The UV luminosity bins have widths of 0.5 mag.

The spectroscopically identified samples rely on higher-resolution NIRSpec data, which are inclusive of AGN with narrower lines and systems where the AGN does not necessarily dominate the total light output.

We emphasize that the UV light is a small fraction of the total luminosity due to the large reddening values and has an unknown origin in either scattered or transmitted AGN light or low-level unobscured star formation. Thus, while useful to put our targets into context, the UV luminosity function does not truly describe the physical properties of the AGN in this sample. For this reason, we also present a bolometric luminosity function in Table 5 and Figure 8. Since the derivation of completeness as a function of bolometric luminosity is not straightforward and would require detailed

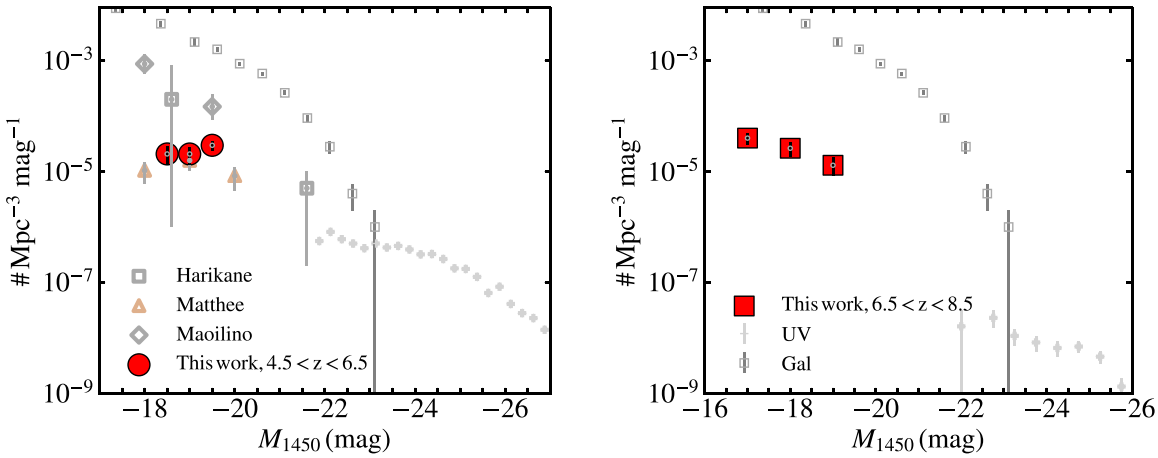

Figure 7. UV luminosity function as measured at 1450 Å. We show the luminosity function in two redshift bins, $4.5 < z < 6.5$ in red circles and $6.5 < z < 8.5$ in red squares. We compare with the UV-selected luminosity functions from Akiyama et al. (2018; left) and Matsuoka et al. (2023; right). We show other JWST-selected broad-line AGN from Harikane et al. (2023), Maiolino et al. (2023), and Matthee et al. (2023). Finally, we compare with the galaxy luminosity function from Bouwens et al. (2017). Consistent with Harikane et al. (2023), we find that the reddened AGN account for ∼20% of the broad-line objects at this redshift, and a few percent of the galaxy population. Our AGN are far more numerous than the UV-selected ones, although they have overlapping bolometric luminosities.

SED modeling in the completeness simulations, we here use the fact that our sample is mostly complete in UV luminosity (see above) to approximate the effective volume for the bolometric luminosity function by assuming the maximum $M_{\rm UV}$ completeness derived above in each $L_{\rm bol}$ bin (of width 1 dex) and no magnification, i.e., the effective volume element is integrated over the whole UNCOVER source plane area of ∼27 arcmin^2 (see Atek et al. 2023b; Furtak et al. 2023c). While this is a reasonable approximation given the properties of our sample, the thus derived bolometric luminosity function remains a lower limit. The lower luminosity bins in particular are probably underestimated since these would be more sensitive to magnification.

To guide our interpretation, we also calculate theoretical black hole bolometric luminosity functions using a combination of high- and low-redshift observations. We consider a galaxy stellar mass function derived by tuning the halo mass function in order to reproduce the evolving observed stellar mass function at $z \sim 4$–7 (for details see Dayal & Giri 2024). We then assign AGN to galaxies, by assuming scaling relations and Eddington ratio distributions. In a "maximal" model we consider the black hole and stellar mass relation at $z \sim 0$ from Reines & Volonteri (2015), valid for high stellar mass elliptical galaxies, $\log(M_{\rm BH}) = 1.4\ \log(M_*) - 6.45$, with a scatter of 0.5 dex, and that all black holes radiate at the Eddington luminosity (Figure 8, "Max"). This maximal line is considerably higher than the compact red sources presented here at $4.5 < z < 6.5$, but our measurements are getting close to the maximal model in our higher-redshift $6.5 < z < 8.5$ bin.

Based on previous theoretical works (Dubois et al. 2015; Bower et al. 2017) finding suppressed Eddington accretion rate for black holes in low-mass galaxies/halos, we limit the Eddington accretion rate to 10^{-2} for halos with masses below $M_{\rm h} = 10^{11}\ M_\odot$. This suppression eases the typical overproduction of the faint end of the AGN luminosity function generally found in models (Habouzit et al. 2017), but does not affect the luminosity range of the AGN in this paper. In fact, in some models showing suppression at low mass, black holes still appear to grow by $z \sim 6$–8 to the moderate black hole masses found here and in other JWST searches (e.g., Trinca et al. 2023). On the other hand, the overproduction motivating this change was based on UV and X-ray luminosity functions, and should be revisited in the JWST era (e.g., Harikane et al. 2023; Maiolino et al. 2023).

Table 5
Bolometric Luminosity Functions of Our Sample of Red AGN

$\log(L_{\rm bol}/{\rm erg\ s^{-1}})$	N	$\phi(L_{\rm bol})$ (Mpc^{-3} dex^{-1})
$z \sim 5$–6 sample		
44.0	1	$(1.0 \pm 0.4) \times 10^{-5}$
45.0	4	$(4.2 \pm 0.7) \times 10^{-5}$
46.0	1	$(1.0 \pm 0.6) \times 10^{-5}$
$z \sim 7$–8 sample		
45.0	2	$(2.6 \pm 0.5) \times 10^{-5}$
46.0	1	$(1.3 \pm 0.5) \times 10^{-5}$

Note. The bins have widths of 1 dex.

We also include luminosity functions from semianalytical models that grow black holes self-consistently starting from a mixture of light and heavy seeds (CAT and Delphi, respectively; Dayal et al. 2019; Trinca et al. 2022). The predicted number densities are lower than inferred from the JWST-discovered AGN, but the models were tuned to reproduce the pre-JWST luminosity functions, which underestimate the number density of the AGN in this sample. Broadly speaking, theoretical models produced more high-redshift faint AGN than observed pre-JWST (Shen et al. 2020, Figure 8, "x"symbols). For a compilation of results see Habouzit et al. (2022).

To explore whether it is possible to reproduce the observed number densities with reasonable assumptions, we finally consider, for the same galaxy mass function, the set of parameters used in Volonteri et al. (2017) to reproduce the best joint $z = 6$ X-ray and UV AGN luminosity functions known at the time: the relation $\log(M_{\rm BH}) = 1.05\ \log(M_*) - 4.1$, valid for moderate-luminosity AGN in low-mass halos, with a scatter of 0.5 dex, an active fraction of 0.25 and a lognormal distribution of the Eddington ratio with mean log(0.40) and $\sigma = 0.40$ (Figure 8, Volonteri et all 2017; V17). We further

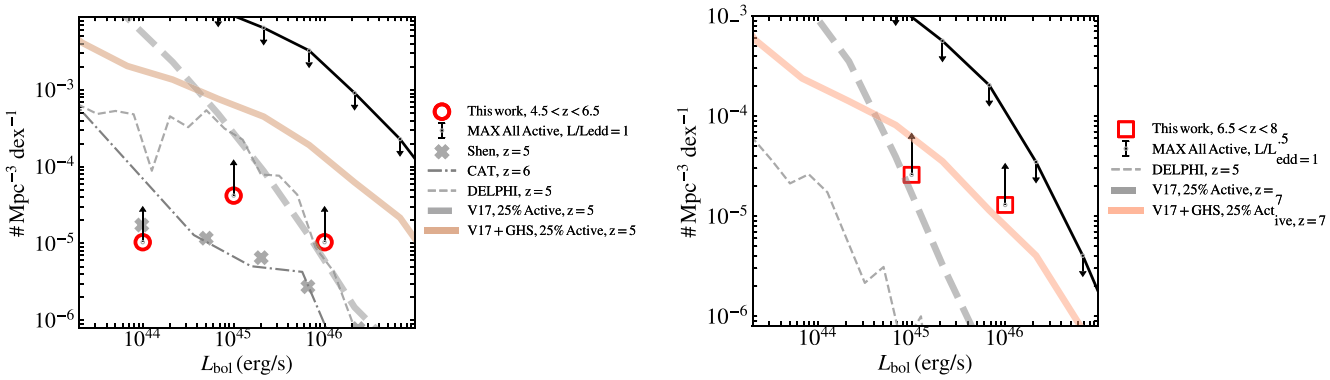

Figure 8. Bolometric AGN luminosity functions ($4.5 < z < 6.5$ top, $6.5 < z < 8.5$ bottom) as inferred from $L_{\rm H\alpha}$ (Table 3). The number densities are lower limits, particularly at low bolometric luminosity where our search will be particularly insensitive to galaxy-dominated objects. We include a maximal bolometric luminosity function assuming that every galaxy harbors an accreting black hole radiating at its Eddington limit and a high normalization of the black hole–galaxy mass relation. Two additional curves based on Volonteri et al. (2017) show cases with an AGN fraction of 0.25 and black hole–galaxy mass relations with lower normalization and different scatter; see text for details. Pre-JWST comparisons are in gray, including the original Volonteri et al. (2017) model, while the updated Volonteri et al. (2017) model is shown in red to indicate JWST inspiration. The pre-JWST bolometric luminosity function compiled by Shen et al. (2020) is shown (gray x). The luminosity functions derived in semianalytical models that grow black holes from seeds are also included as gray lines (Cosmic Archaeology Tool (CAT) and Delphi, respectively; Dayal et al. 2019; Trinca et al. 2022).

consider the single fit to all black holes in Greene et al. (2020) $\log(M_{\rm BH}) = 1.39\ \log(M_*) - 7.38$, with a scatter of 0.8 dex and using the same active fraction and Eddington ratio distribution as V17 (Figure 8, V17 and Greene, Strader, & Ho; GHS). With these models we find that the number density of AGN can be accommodated in relation to the galaxy population, taking into account the scatter in the scaling relations and an active fraction of about 25%, but again overproducing AGN relative to Shen et al. (2020). In summary, pre-JWST models tended to overproduce AGN, while it seems plausible to reproduce the JWST-observed number densities with reasonable assumptions, but many details (like the distribution of black hole to galaxy mass) remain to studied in more detail.

6.3. Black Hole Masses

We follow Greene & Ho (2005), as updated by Reines et al. (2013), to calculate the black hole masses based on the luminosity $L_{\rm H\alpha}$ and velocity FWHM(Hα) of the broad Hα line. These single-epoch black hole mass estimates (e.g., Shen et al. 2019) are based on assuming that the BLR acts as a dynamical tracer of the black hole (e.g., Pancoast et al. 2014). The size of the BLR is estimated from the AGN luminosity (e.g., Bentz et al. 2013), and then assuming virial equilibrium, the dynamical mass scales as $M_{\rm BH} \propto {\rm FWHM}^2_{\rm H\alpha} R$. We have taken a value of $\epsilon = 1$, where the typical f-factor is calibrated to the velocity dispersion of the line while ϵ is calibrated to the FWHM used here (e.g., Onken et al. 2004; Pancoast et al. 2014). Of course, we do not know that the BLR is in virial equilibrium, nor do we know whether we probe the velocity field at a comparable radius as the BLR "size" we estimate from the luminosity (e.g., Krolik 2001; Linzer et al. 2022).

The black hole masses are plotted against the UV luminosities and the Hα-inferred bolometric luminosities in Figure 9. We compare the sources both to luminous UV-selected quasars from the review of Fan et al. (2023) and to recent moderate-luminosity broad-line AGN discovered with JWST (Barro et al. 2023; Harikane et al. 2023; Kocevski et al. 2023; Matthee et al. 2023). Our sources are on the massive end of the broad-line AGN found in deep JWST fields, but barely reach the low end of the black hole masses and luminosities seen in the rare UV-selected sources. However, their UV luminosities are 4–5 mag lower than the UV-selected AGN at comparable $M_{\rm BH}$. This difference is very likely due to dust obscuration. As shown on the right-hand side, when we use the broad emission lines with dust correction to estimate the bolometric luminosity, we find much more agreement in the luminosity ranges at a given $M_{\rm BH}$.

It is worth noting MSAID45924. This galaxy is the brightest in the sample (F444W = 22 mag) and stands out for its high S/N and black hole mass of $M_{\rm BH} \approx 10^9\ M_\odot$. The object warrants bespoke analysis that is beyond the scope of this work.

7. Discussion and Summary

In this work, we present NIRSpec/PRISM spectroscopic follow up of 15 red, compact sources selected in the UNCOVER A2744 field. The majority of these targets are confirmed to be AGN with $z > 4.5$. The UV/optical SEDs have a characteristic steep red continuum toward the rest-frame optical but also a nonnegligible UV component. The rest-frame optical is consistent with a reddened ($A_V \sim 1.5$) broad-line AGN. The UV slopes are well fit as unobscured AGN in slope, but suppressed by $\sim$100 times relative to an unreddened source. From the available low-resolution spectroscopy and broadband SED data, we cannot rule out that the UV component is due to moderately reddened star formation at the level of a few solar masses per year in the host. AGN with similar shapes (Noboriguchi et al. 2023) are known at all redshifts (e.g., Glikman et al. 2012; Banerji et al. 2015; Veilleux et al. 2016; Hamann et al. 2017; Assef et al. 2018; Pan et al. 2021). However, at $z < 3$, these reddened sources with a UV excess are rare; Noboriguchi et al. (2019) estimate that of all the dust-obscured AGN, only 1% have a UV excess.

JWST is uncovering a surprisingly high number density of red AGN at $z > 5$ (see also Harikane et al. 2023; Barro et al. 2023; Matthee et al. 2023; L23). This high number density is unexpected compared to UV-selected sources, which have measured number densities nearly 100 times lower at their faintest UV luminosities (e.g., Matsuoka et al. 2018, 2023), although nominally the densities are similar to some X-ray selections (Giallongo et al. 2019). However, these sources are not detected in the X-ray. Specifically, while the Matthee et al. (2023)

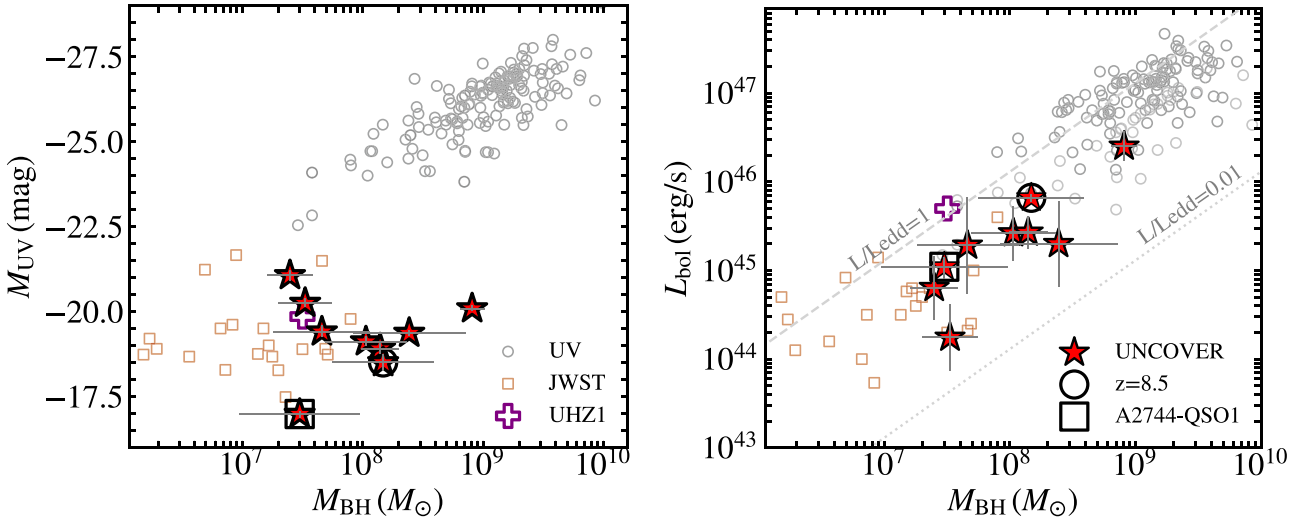

Figure 9. Black hole mass vs. M_{UV} (left) and bolometric luminosity (right) for the broad-line AGN (red stars) including A2744-QSO1 (Furtak et al. 2023a, 2023b; red star and square) and the source MSAID20466 at $z = 8.5$ (Kokorev et al. 2023; red star and open circle). For context, we include the UV-selected AGN with $z > 5$ from Fan et al. (2023), other JWST-selected broad-line sources (Harikane et al. 2023; Maiolino et al. 2023; Matthee et al. 2023), and the X-ray–detected AGN at $z = 10.07$, UHZ1 (Bogdan et al. 2024; Goulding et al. 2023). Note that our sources extend to surprisingly high $M_{BH} = 10^9\ M_\odot$.

objects may be too faint to detect, the triply lensed source in the UNCOVER field is inferred to be 10 times weaker in the X-ray than expected given the optical observations (Furtak et al. 2023b). Additionally, the compact red AGN account for a large fraction of all red-selected sources with JWST. After applying simple color cuts designed to select massive galaxies (as in Labbé et al. 2023b), our spectra imply that at least one-third of the selected objects will be AGN. This number rises to nearly 100% for the reddest tail of sources (F277 – F444W > 1.6), and is also >80% when we apply a compactness criterion and enforce a red power-law continuum.

One of the intriguing aspects of these compact red sources is the low galaxy masses that are implied by their compact sizes (e.g., Izumi et al. 2019; Furtak et al. 2023b; Kokorev et al. 2023). Of course, we are selecting only point sources, which necessarily biases the sample toward those with high a black hole to galaxy ratio. Furthermore, Volonteri et al. (2023) suggest that color selections would indeed preferentially identify black holes that are overmassive with respect to the galaxy due to the requirement that the AGN dominate over the galaxy light. However, the high number densities that we and others find for such targets means that a significant fraction of the black hole population is likely to have outgrown their hosts; this high level of scatter is also required to match the bolometric luminosity functions (Section 6.2). An important caveat is of course that we do not yet know the bolometric luminosities of these sources. They rely on a very model-dependent interpretation of the spectra that implies very high dust reddening.

While it is true that the high inferred number densities can be generally accommodated assuming reasonable AGN fractions and scalings with the galaxy population, a widespread efficient growth of black holes starting from initial conditions, "seeds," remains to be explained. There are a few ways to imagine growing a large enough black hole mass density this early. Black hole seeds could form heavy ($M_{BH} \sim 10^4\ M_\odot$) as in direct collapse models (Loeb & Rasio 1994; Bromm & Loeb 2003; Lodato & Natarajan 2006; Begelman et al. 2008; Visbal et al. 2014; Habouzit et al. 2016) or in dense star clusters (e.g., Portegies Zwart & McMillan 2002; Omukai et al. 2008; Devecchi & Volonteri 2009; Mapelli 2016; Natarajan 2021; Schleicher et al. 2022). With heavy seeds, it is easier to grow the black hole more rapidly than the galaxy (Trinca et al. 2022), although classic "direct collapse" models cannot make high number densities of heavy seeds (Dayal et al. 2019; Inayoshi et al. 2022). Recent simulations suggest that rapidly growing halos have conditions where somewhat less massive seeds form, $\sim 10^4\ M_\odot$, but in larger numbers and in the presence of a relatively dense stellar distribution (Regan et al. 2020). Models invoking boosted growth from surrounding star clusters would then help the seeds grow relatively early (e.g., Alexander & Natarajan 2014; Natarajan 2021).

Alternatively, all of the black holes could start as light seeds (Fryer et al. 2001; Madau & Rees 2001; Bromm & Larson 2004), with some of them able to grow at super-Eddington rates to make the high mass density of black holes (e.g., Madau et al. 2014). Some super-Eddington accretion, irrespective of the type of seed, is favored by the semiempirical model TRINITY (Zhang et al. 2023b), which uses halo statistics and an observation-driven Bayesian framework to model galaxy and black hole growth jointly. At the same time, detailed magnetohydrodynamical simulations do find viable super-Eddington accretion flows (e.g., Jiang et al. 2019).

Super-Eddington accretion may also explain some of the SED properties of the compact red sources, in particular the apparently low X-ray luminosities. It is even possible that the red continuum could be explained by super-Eddington accretion if the inner accretion flow grows optically thick but leaves an outer disk. Super-Eddington accretion would also alleviate the tension with our "maximal" model, but producing more luminosity for a given black hole mass.

One other complication may come from mergers. At low redshifts, reddened broad-line AGN seem to reside preferentially in merging hosts (e.g., Urrutia et al. 2008). If the red sources presented here were also dominated by merging hosts, then perhaps the merging system may be harder to detect than an undisturbed galaxy due to variable extinction and perhaps a significant low surface brightness component. There could also be two AGN powering the objects in some cases in principle. Notionally, the number densities of major mergers at $z \sim 6$

could be high enough to match the number density of the compact red sources. Taking an empirically motivated merger timescale ~ 0.5 Gyr and a merger volume density ~ 3–5×10^{-5} Mpc^{-3} Gyr^{-1} for $M_* \approx 10^9$–10^{10} $M_\odot$ galaxies from empirical halo modeling (O'Leary et al. 2021), we estimate $\sim 2 \times 10^{-5}$ Mpc^{-3} mergers at $5 < z < 6$. Plausibly then there could be a relationship between AGN triggering, merging, and the observed reddening. As was seen in Matthee et al. (2023), the compact red sources also appear to be clustered with each other. Fujimoto et al. (2023a) highlights a potential overdensity hinted at by a compact red AGN and a UV-bright object found together in the same giant ionized bubble with a radius of 7.69 ± 0.18 proper Mpc at $z = 8.5$. Perhaps this excess clustering could be related to a merger origin for these sources.

An obvious additional question is the possible role of these sources in reionization. Depending on the (poorly understood) number densities and accretion rates of black holes compared to star-forming galaxies at the faint end of the UV luminosity function, they could either have made a minimal contribution (a few tens of percent; Hassan et al. 2018; Dayal et al. 2020; Trebitsch et al. 2021; Finkelstein & Bagley 2022) or dominate the photon budget for reionization (e.g., Madau & Haardt 2015; Grazian et al. 2018). Revisiting the role of moderate-luminosity AGN in reionization is in order, although the red objects considered here may not produce many ionizing photons.

There are many additional puzzles raised by the "little red dots," including their apparent clustering, their unique SEDs (characteristic red optical continuum, an additional UV component, and a lack of X-ray emission), and their possible lack of significant host galaxy component. These red broad-line AGN apparently constitute a sizable 10%–20% fraction of broad-line AGN at $z > 5$, as well as a sizable fraction of red galaxies at the same epoch. They are an important part of the story of black hole growth at early times.

Acknowledgments

J.E.G. and A.D.G acknowledge support from NSF/AAG grant No. 1007094, and J.E.G. also acknowledges support from NSF/AAG grant No. 1007052. A.Z. acknowledges support by grant No. 2020750 from the United States-Israel Binational Science Foundation (BSF) and grant No. 2109066 from the United States National Science Foundation (NSF), and by the Ministry of Science & Technology of Israel. The Cosmic Dawn Center is funded by the Danish National Research Foundation (DNRF) under grant No. 140. This work has received funding from the Swiss State Secretariat for Education, Research and Innovation (SERI) under contract number MB22.00072, as well as from the Swiss National Science Foundation (SNSF) through project grant 200020_207349. P.D. acknowledges support from the NWO grant 016.VIDI.189.162 ("ODIN") and from the European Commission's and University of Groningen's CO-FUND Rosalind Franklin program. K.G. and T.N. acknowledge support from Australian Research Council Laureate Fellowship FL180100060. H.A. and I.C. acknowledge support from CNES, focused on the JWST mission, and the Programme National Cosmology and Galaxies (PNCG) of CNRS/INSU with INP and IN2P3, cofunded by CEA and CNES. R.P.N. acknowledges funding from JWST programs GO-1933 and GO-2279. Support for this work was provided by NASA through the NASA Hubble Fellowship grant HST-HF2-51515.001-A awarded by the Space Telescope Science Institute, which is operated by the Association of Universities for Research in Astronomy, Incorporated, under NASA contract NAS5-26555. The research of C.C.W. is supported by NOIRLab, which is managed by the Association of Universities for Research in Astronomy (AURA) under a cooperative agreement with the National Science Foundation. B.W. acknowledges support from JWST-GO-02561.022-A. A.J.B. acknowledges funding support from NASA/ADAP grant 21-ADAP21-0187. Support for this work was provided by The Brinson Foundation through a Brinson Prize Fellowship grant. R.P.N. acknowledges support for this work provided by NASA through the NASA Hubble Fellowship grant HST-HF2-51515.001-A awarded by the Space Telescope Science Institute, which is operated by the Association of Universities for Research in Astronomy, Incorporated, under NASA contract NAS5-26555. C.P. thanks Marsha and Ralph Schilling for the generous support of this research.

ORCID iDs

Jenny E. Greene https://orcid.org/0000-0002-5612-3427
Ivo Labbe https://orcid.org/0000-0002-2057-5376
Andy D. Goulding https://orcid.org/0000-0003-4700-663X
Lukas J. Furtak https://orcid.org/0000-0001-6278-032X
Iryna Chemerynska https://orcid.org/0009-0009-9795-6167
Vasily Kokorev https://orcid.org/0000-0002-5588-9156
Pratika Dayal https://orcid.org/0000-0001-8460-1564
Marta Volonteri https://orcid.org/0000-0002-3216-1322
Christina C. Williams https://orcid.org/0000-0003-2919-7495
Bingjie Wang (王冰洁) https://orcid.org/0000-0001-9269-5046
David J. Setton https://orcid.org/0000-0003-4075-7393
Adam J. Burgasser https://orcid.org/0000-0002-6523-9536
Rachel Bezanson https://orcid.org/0000-0001-5063-8254
Hakim Atek https://orcid.org/0000-0002-7570-0824
Gabriel Brammer https://orcid.org/0000-0003-2680-005X
Sam E. Cutler https://orcid.org/0000-0002-7031-2865
Robert Feldmann https://orcid.org/0000-0002-1109-1919
Seiji Fujimoto https://orcid.org/0000-0001-7201-5066
Karl Glazebrook https://orcid.org/0000-0002-3254-9044
Anna de Graaff https://orcid.org/0000-0002-2380-9801
Gourav Khullar https://orcid.org/0000-0002-3475-7648
Joel Leja https://orcid.org/0000-0001-6755-1315
Danilo Marchesini https://orcid.org/0000-0001-9002-3502
Michael V. Maseda https://orcid.org/0000-0003-0695-4414
Jorryt Matthee https://orcid.org/0000-0003-2871-127X
Tim B. Miller https://orcid.org/0000-0001-8367-6265
Rohan P. Naidu https://orcid.org/0000-0003-3997-5705
Themiya Nanayakkara https://orcid.org/0000-0003-3997-5705
Pascal A. Oesch https://orcid.org/0000-0001-5851-6649
Richard Pan https://orcid.org/0000-0002-9651-5716
Casey Papovich https://orcid.org/0000-0001-7503-8482
Sedona H. Price https://orcid.org/0000-0002-0108-4176
Pieter van Dokkum https://orcid.org/0000-0002-8282-9888
John R. Weaver https://orcid.org/0000-0003-1614-196X
Katherine E. Whitaker https://orcid.org/0000-0001-7160-3632
Adi Zitrin https://orcid.org/0000-0002-0350-4488

References

Abel, N. P., & Satyapal, S. 2008, ApJ, 678, 686
Akins, H. B., Casey, C. M., Allen, N., et al. 2023, ApJ, 956, 61
Akiyama, M., He, W., Ikeda, H., et al. 2018, PASJ, 70, S34
Alexander, T., & Natarajan, P. 2014, Sci, 345, 1330

Amaro-Seoane, P., Andrews, J., Arca Sedda, M., et al. 2023, LRR, 26, 2
Assef, R. J., Stern, D., Kochanek, C. S., et al. 2013, ApJ, 772, 26
Assef, R. J., Stern, D., Noirot, G., et al. 2018, ApJS, 234, 23
Atek, H., Labbé, I., Furtak, L. J., et al. 2023a, arXiv:2308.08540
Atek, H., Chemerynska, I., Wang, B., et al. 2023b, MNRAS, 524, 5486
Atek, H., Richard, J., Kneib, J. P., & Schaerer, D. 2018, MNRAS, 479, 5184
Baggen, J. F. W., van Dokkum, P., Labbe, I., et al. 2023, ApJL, 955, L12
Bañados, E., Venemans, B. P., Mazzucchelli, C., et al. 2018, Natur, 553, 473
Banerji, M., Alaghband-Zadeh, S., Hewett, P. C., & McMahon, R. G. 2015, MNRAS, 447, 3368
Barro, G., Perez-Gonzalez, P. G., Kocevski, D. D., et al. 2023, arXiv:2305.14418
Baskin, A., & Laor, A. 2005, MNRAS, 358, 1043
Begelman, M. C., Rossi, E. M., & Armitage, P. J. 2008, MNRAS, 387, 1649
Bentz, M. C., Denney, K. D., Grier, C. J., et al. 2013, ApJ, 767, 149
Bergamini, P., Acebron, A., Grillo, C., et al. 2023, ApJ, 952, 84
Bezanson, R., Labbe, I., Whitaker, K. E., et al. 2022, arXiv:2212.04026
Bhatawdekar, R., & Conselice, C. J. 2021, ApJ, 909, 144
Binette, L., Villar Martín, M., Magris, C., et al. 2022, RMxAA, 58, 133
Bogdan, A., Goulding, A., Natarajan, P., et al. 2024, NatAs, 8, 126
Bouwens, R. J., Aravena, M., Decarli, R., et al. 2016, ApJ, 833, 72
Bouwens, R. J., Oesch, P. A., Illingworth, G. D., Ellis, R. S., & Stefanon, M. 2017, ApJ, 843, 129
Bower, R. G., Schaye, J., Frenk, C. S., et al. 2017, MNRAS, 465, 32
Brammer, G. 2022, msaexp: NIRSpec analysis tools, v0.3.4, Zenodo, doi:10.5281/zenodo.7299500
Bromm, V., & Larson, R. B. 2004, ARA&A, 42, 79
Bromm, V., & Loeb, A. 2003, ApJ, 596, 34
Burgasser, A. J., Gerasimov, R., Bezanson, R., et al. 2024, ApJ, 962, 177
Carnall, A. C., McLure, R. J., Dunlop, J. S., & Davé, R. 2018, MNRAS, 480, 4379
Carnall, A. C., McLure, R. J., Dunlop, J. S., et al. 2019, MNRAS, 490, 417
Croom, S. M., Rhook, K., Corbett, E. A., et al. 2002, MNRAS, 337, 275
Davis, S. W., Woo, J. H., & Blaes, O. M. 2007, ApJ, 668, 682
Dayal, P., & Giri, S. K. 2024, MNRAS, 528, 2784
Dayal, P., Rossi, E. M., Shiralilou, B., et al. 2019, MNRAS, 486, 2336
Dayal, P., Volonteri, M., Choudhury, T. R., et al. 2020, MNRAS, 495, 3065
de Graaff, A., Rix, H. W., Carniani, S., et al. 2023, arXiv:2308.09742
Devecchi, B., & Volonteri, M. 2009, ApJ, 694, 302
Donley, J. L., Koekemoer, A. M., Brusa, M., et al. 2012, ApJ, 748, 142
Dubois, Y., Volonteri, M., Silk, J., et al. 2015, MNRAS, 452, 1502
Endsley, R., Stark, D. P., Lyu, J., et al. 2023, MNRAS, 520, 4609
Endsley, R., Stark, D. P., Whitler, L., et al. 2022, arXiv:2208.14999
Fan, X., Banados, E., & Simcoe, R. A. 2023, ARA&A, 61, 373
Fan, X., Wang, F., Yang, J., et al. 2019, ApJL, 870, L11
Finkelstein, S. L., & Bagley, M. B. 2022, ApJ, 938, 25
Fryer, C. L., Woosley, S. E., & Heger, A. 2001, ApJ, 550, 372
Fujimoto, S., Brammer, G. B., Watson, D., et al. 2022, Natur, 604, 261
Fujimoto, S., Kohno, K., Ouchi, M., et al. 2023b, arXiv:2303.01658
Fujimoto, S., Wang, B., Weaver, J., et al. 2023a, arXiv:2308.11609
Fumagalli, M., Patel, S. G., Franx, M., et al. 2012, ApJL, 757, L22
Furtak, L. J., Labbé, I., Zitrin, A., et al. 2023b, arXiv:2308.05735
Furtak, L. J., Zitrin, A., Plat, A., et al. 2023a, ApJ, 952, 142
Furtak, L. J., Zitrin, A., Weaver, J. R., et al. 2023c, MNRAS, 523, 4568
Gardner, J. P., Mather, J. C., Abbott, R., et al. 2023, PASP, 135, 068001
Giallongo, E., Grazian, A., Fiore, F., et al. 2019, ApJ, 884, 19
Glikman, E., Urrutia, T., Lacy, M., et al. 2012, ApJ, 757, 51
Gordon, K. D., Clayton, G. C., Misselt, K. A., Landolt, A. U., & Wolff, M. J. 2003, ApJ, 594, 279
Goulding, A. D., Greene, J. E., Setton, D. J., et al. 2023, ApJL, 955, L24
Grazian, A., Giallongo, E., Boutsia, K., et al. 2018, A&A, 613, A44
Greene, J. E., & Ho, L. C. 2005, ApJ, 630, 122
Greene, J. E., Strader, J., & Ho, L. C. 2020, ARA&A, 58, 257
Habouzit, M., Somerville, R. S., Li, Y., et al. 2022, MNRAS, 509, 3015
Habouzit, M., Volonteri, M., & Dubois, Y. 2017, MNRAS, 468, 3935
Habouzit, M., Volonteri, M., Latif, M., Dubois, Y., & Peirani, S. 2016, MNRAS, 463, 529
Hainline, K. N., Helton, J. M., Johnson, B. D., et al. 2023b, arXiv:2309.03250
Hainline, K. N., Johnson, B. D., Robertson, B., et al. 2023a, arXiv:2306.02468
Hamann, F., Zakamska, N. L., Ross, N., et al. 2017, MNRAS, 464, 3431
Hao, L., Strauss, M. A., Tremonti, C. A., et al. 2005, AJ, 129, 1783
Harikane, Y., Ono, Y., Ouchi, M., et al. 2022, ApJS, 259, 20
Harikane, Y., Zhang, Y., Nakajima, K., et al. 2023, ApJ, 959, 39
Hassan, S., Davé, R., Mitra, S., et al. 2018, MNRAS, 473, 227
Hinshaw, G., Larson, D., Komatsu, E., et al. 2013, ApJS, 208, 19
Horne, K. 1986, PASP, 98, 609
Inayoshi, K., Onoue, M., Sugahara, Y., Inoue, A. K., & Ho, L. C. 2022, ApJL, 931, L25
Inayoshi, K., Visbal, E., & Haiman, Z. 2020, ARA&A, 58, 27
Izotov, Y. I., Thuan, T. X., & Privon, G. 2012, MNRAS, 427, 1229
Izumi, T., Onoue, M., Matsuoka, Y., et al. 2019, PASJ, 71, 111
Jakobsen, P., Ferruit, P., Alves de Oliveira, C., et al. 2022, A&A, 661, A80
Jiang, Y. F., Stone, J. M., & Davis, S. W. 2019, ApJ, 880, 67
Kocevski, D. D., Onoue, M., Inayoshi, K., et al. 2023, ApJL, 954, L4
Kokorev, V., Fujimoto, S., Labbe, I., et al. 2023, ApJL, 957, L7
Korista, K. T., & Goad, M. R. 2004, ApJ, 606, 749
Krolik, J. H. 2001, ApJ, 551, 72
Labbé, I., Greene, J. E., Bezanson, R., et al. 2023a, arXiv:2306.07320
Labbé, I., van Dokkum, P., Nelson, E., et al. 2023b, Natur, 616, 266
Langeroodi, D., & Hjorth, J. 2023, ApJL, 957, L27
Larson, R. L., Finkelstein, S. L., Kocevski, D. D., et al. 2023, ApJL, 953, L29
Leung, G. C. K., Bagley, M. B., Finkelstein, S. L., et al. 2023, ApJL, 954, L46
Leung, G. C. K., Coil, A. L., Rupke, D. S. N., & Perrotta, S. 2021, ApJ, 914, 17
Linzer, N. B., Goulding, A. D., Greene, J. E., & Hickox, R. C. 2022, ApJ, 937, 65
Liu, X., Zakamska, N. L., Greene, J. E., et al. 2009, ApJ, 702, 1098
Lodato, G., & Natarajan, P. 2006, MNRAS, 371, 1813
Loeb, A., & Rasio, F. A. 1994, ApJ, 432, 52
Lotz, J. M., Koekemoer, A., Coe, D., et al. 2017, ApJ, 837, 97
Madau, P., & Haardt, F. 2015, ApJL, 813, L8
Madau, P., Haardt, F., & Dotti, M. 2014, ApJL, 784, L38
Madau, P., & Rees, M. J. 2001, ApJL, 551, L27
Maiolino, R., Scholtz, J., Curtis-Lake, E., et al. 2023, arXiv:2308.01230
Mapelli, M. 2016, MNRAS, 459, 3432
Matsuoka, Y., Onoue, M., Iwasawa, K., et al. 2023, ApJL, 949, L42
Matsuoka, Y., Strauss, M. A., Kashikawa, N., et al. 2018, ApJ, 869, 150
Matthee, J., Naidu, R. P., Brammer, G., et al. 2023, arXiv:2306.05448
Meisner, A. M., Schneider, A. C., Burgasser, A. J., et al. 2021, ApJ, 915, 120
Mortlock, D. J., Warren, S. J., Venemans, B. P., et al. 2011, Natur, 474, 616
Nanayakkara, T., Glazebrook, K., Jacobs, C., et al. 2023, ApJL, 947, L26
Natarajan, P. 2021, MNRAS, 501, 1413
Netzer, H. 1990, in Active Galactic Nuclei, ed. R. D. Blandford et al. (Berlin: Springer)
Noboriguchi, A., Inoue, A. K., Nagao, T., Toba, Y., & Misawa, T. 2023, ApJL, 959, L14
Noboriguchi, A., Nagao, T., Toba, Y., et al. 2019, ApJ, 876, 132
Oesch, P. A., Brammer, G., Naidu, R. P., et al. 2023, MNRAS, 525, 2864
O'Leary, J. A., Moster, B. P., Naab, T., & Somerville, R. S. 2021, MNRAS, 501, 3215
Omukai, K., Schneider, R., & Haiman, Z. 2008, ApJ, 686, 801
Onken, C. A., Ferrarese, L., Merritt, D., et al. 2004, ApJ, 615, 645
Ono, Y., Harikane, Y., Ouchi, M., et al. 2023, ApJ, 951, 72
Onoue, M., Inayoshi, K., Ding, X., et al. 2023, ApJL, 942, L17
Osterbrock, D. E. 1977, ApJ, 215, 733
Osterbrock, D. E. 1989, Astrophysics of Gaseous Nebulae and Active Galactic Nuclei (Melville, NY: AIP)
Pan, X., Zhou, H., Yang, C., et al. 2021, ApJ, 912, 118
Pancoast, A., Brewer, B. J., Treu, T., et al. 2014, MNRAS, 445, 3073
Pascale, M., Frye, B. L., Diego, J., et al. 2022, ApJL, 938, L6
Portegies Zwart, S. F., & McMillan, S. L. W. 2002, ApJ, 576, 899
Regan, J. A., Wise, J. H., Woods, T. E., et al. 2020, OJAp, 3, 15
Reines, A. E., Greene, J. E., & Geha, M. 2013, ApJ, 775, 116
Reines, A. E., & Volonteri, M. 2015, ApJ, 813, 82
Schleicher, D. R. G., Reinoso, B., Latif, M., et al. 2022, MNRAS, 512, 6192
Shen, X., Hopkins, P. F., Faucher-Giguère, C. A., et al. 2020, MNRAS, 495, 3252
Shen, Y., Wu, J., Jiang, L., et al. 2019, ApJ, 873, 35
Somalwar, J. J., & Ravi, V. 2023, arXiv:2306.00898
Stern, D., Eisenhardt, P., Gorjian, V., et al. 2005, ApJ, 631, 163
Stern, J., & Laor, A. 2012, MNRAS, 423, 600
Temple, M. J., Hewett, P. C., & Banerji, M. 2021, MNRAS, 508, 737
Topping, M. W., Stark, D. P., Endsley, R., et al. 2023, arXiv:2307.08835
Trebitsch, M., Dubois, Y., Volonteri, M., et al. 2021, A&A, 653, A154
Trebitsch, M., Hutter, A., Dayal, P., et al. 2023, MNRAS, 518, 3576
Trinca, A., Schneider, R., Maiolino, R., et al. 2023, MNRAS, 519, 4753
Trinca, A., Schneider, R., Valiante, R., et al. 2022, MNRAS, 511, 616
Übler, H., Maiolino, R., Curtis-Lake, E., et al. 2023, A&A, 677, A145
Urrutia, T., Lacy, M., & Becker, R. H. 2008, ApJ, 674, 80
Vanden Berk, D. E., Richards, G. T., Bauer, A., et al. 2001, AJ, 122, 549
Veilleux, S., Meléndez, M., Tripp, T. M., Hamann, F., & Rupke, D. S. N. 2016, ApJ, 825, 42

Visbal, E., Haiman, Z., & Bryan, G. L. 2014, MNRAS, 445, 1056
Volonteri, M., Habouzit, M., & Colpi, M. 2023, MNRAS, 521, 241
Volonteri, M., & Reines, A. E. 2016, ApJL, 820, L6
Volonteri, M., Reines, A. E., Atek, H., Stark, D. P., & Trebitsch, M. 2017, ApJ, 849, 155
Wang, B., Fujimoto, S., Labbé, I., et al. 2023, ApJL, 957, L34
Wang, B., Leja, J., Labbé, I., et al. 2024, ApJS, 270, 12
Wang, F., Fan, X., Yang, J., et al. 2021, ApJ, 908, 53
Weaver, J. R., Cutler, S. E., Pan, R., et al. 2024, ApJS, 270, 7
Whitaker, K. E., Franx, M., Leja, J., et al. 2014, ApJ, 795, 104
Yang, G., Caputi, K. I., Papovich, C., et al. 2023, ApJL, 950, L5
York, D. G., Adelman, J., Anderson, J. E. J., et al. 2000, AJ, 120, 1579
Zakamska, N. L., Hamann, F., Pâris, I., et al. 2016, MNRAS, 459, 3144
Zhang, H., Behroozi, P., Volonteri, M., et al. 2023a, MNRAS, 523, L69
Zhang, H., Behroozi, P., Volonteri, M., et al. 2023b, MNRAS, 518, 2123
Zitrin, A., Fabris, A., Merten, J., et al. 2015, ApJ, 801, 44